

1 **Projecting end of century climate extremes and their impacts on the**  
2 **hydrology of a representative California watershed**

3

4 Fadji Z. Maina<sup>1,3\*</sup>, Alan Rhoades<sup>2</sup>, Erica R. Siirila-Woodburn<sup>1</sup>, Peter-James Denny-Frank<sup>1</sup>

5 <sup>1</sup>Energy Geosciences Division, Lawrence Berkeley National Laboratory 1 Cyclotron Road, M.S.  
6 74R-316C, Berkeley, CA 94704, USA

7 <sup>2</sup>Climate and Ecosystem Sciences Division, Lawrence Berkeley National Laboratory 1  
8 Cyclotron Road, M.S. 74R-316C, Berkeley, CA 94704, USA

9 <sup>3</sup> now at NASA Goddard Space Flight Center, Hydrological Sciences Laboratory, Greenbelt,  
10 MD, USA

11

12

13 \*Corresponding Author: [fadjizaouna.maina@nasa.gov](mailto:fadjizaouna.maina@nasa.gov)

14 **Abstract**

15           In California, it is essential to understand the evolution of water resources in response to a  
16 changing climate to sustain its economy and agriculture and to build resilient communities.  
17 Although extreme conditions have characterized the historical hydroclimate of California, climate  
18 change will likely intensify hydroclimatic extremes by the End of Century (EoC). However, few  
19 studies have investigated the impacts of EoC extremes on watershed hydrology. We use cutting-  
20 edge global climate and integrated hydrologic models to simulate EoC extremes and their effects  
21 on the water-energy balance. We assess the impacts of projected driest, median, and wettest water  
22 years under a Representative Concentration Pathway (RCP) 8.5 on the hydrodynamics of the  
23 Cosumnes river basin. Substantial changes to annual average temperature ( $>+2.5^{\circ}\text{C}$ ) and  
24 precipitation ( $>+38\%$ ) will characterize the EoC extreme water years compared to their historical  
25 counterparts. A shift in the dominant form of precipitation, mostly in the form of rain, is projected  
26 to fall earlier. These changes reduce snowpack by more than 90%, increase peak surface water and  
27 groundwater storages up to 75% and 23%, respectively, and drive the timing of peak storage to  
28 occur earlier in the year. Because EoC temperatures and soil moisture are high, both potential and  
29 actual evapotranspiration (*ET*) increase. The latter, along with the lack of snowmelt in the warm  
30 EoC, cause surface water and groundwater storages to significantly decrease in summer, with  
31 groundwater showing the highest rates of decrease. These changes result in more ephemeral EoC  
32 streams with more focused flow and increased storage in the mainstem of the river network during  
33 the summer.

34 **Keywords:** future climate extremes, integrated hydrologic model, global climate model, end of  
35 century hydrology, watershed hydrology, water management

36           **Introduction**

37           California, the fifth\*largest economy in the world, hosts one of the largest agricultural  
38 regions in the United States and is home to over 39 million people. Because of its geographic  
39 location, Mediterranean climate, geology, and landscape, the state of California is sensitive to  
40 climate change (Hayhoe et al. 2004). Understanding how water resources will evolve under a  
41 changing climate is crucial for sustaining the state’s economy and agricultural productivity. The  
42 region is especially susceptible to climate change given its reliance on the Sierra Nevada Mountain  
43 snowpack as a source of water supply (e.g., Dettinger & Anderson, 2015). Studies show that  
44 temperatures may warm by as much as 4.5°C by the End of Century (hereafter, EoC) (Cayan et  
45 al., 2008), that snowpack is expected to decrease as most precipitation will fall as rain instead of  
46 snow (Siirila-Woodburn, et al., 2021), and that rain on snow events will exacerbate melt (Cayan  
47 et al., 2008; Gleick, 1987; Maurer, 2007; Mote et al., 2005; Musselman, Clark, et al., 2017;  
48 Musselman, Molotch, et al., 2017; Rhoades, Ullrich, & Zarzycki, 2018a). Given that precipitation  
49 falls predominantly in winter months and the summers are hot and dry, the snow accumulated  
50 during the winter provides important water storage for the dry season and is crucial to meet urban  
51 demand, sustain ecosystem function, and maintain agricultural productivity (Bales et al., 2006;  
52 Dierauer et al., 2018). As such, any significant reduction in the snowpack has the potential to  
53 drastically affect the hydrology of the state (Barnett et al., 2005; Harpold & Molotch, 2015; Milly  
54 et al., 2005; Rhoades et al., 2018 a,b).

55           Over the past several decades, researchers have worked to understand how changes in  
56 Sierra Nevada snowpack will affect important hydrologic fluxes such as evapotranspiration (Tague  
57 & Peng, 2013) and streamflow (Berghuijs et al., 2014; Gleick, 1987; He et al., 2019; Maurer, 2007;  
58 Safeeq et al., 2014; Son & Tague, 2019; Vicuna & Dracup, 2007; Vicuna et al., 2007). For

59 example, analyses of recent historical trends show that reductions in snowpack result in increases  
60 in winter streamflow and decreases in the summer streamflow (e.g. Safeeq et al., 2012). However,  
61 the sensitivity of a given area to these climatic changes depends on many factors including geology  
62 and therefore drainage efficiency, topography, and land cover (Alo & Wang, 2008; Christensen et  
63 al., 2008; Cristea et al., 2014; Ficklin et al., 2013; Mayer & Naman, 2011; Safeeq et al., 2015; Son  
64 & Tague, 2019; Tang et al., 2019).

65 Climate change in California is also expected to lead to unprecedented extreme conditions,  
66 which include both severe drought and intense deluge (Swain et al., 2018). In recent years, these  
67 changes have already been observed in the forms of multi-year droughts (Cook et al., 2004; Griffin  
68 & Anchukaitis, 2014; Shukla et al., 2015) and high-intensity precipitation events mainly caused  
69 by atmospheric rivers (Dettinger et al., 2004; Dettinger, 2011; Dettinger, 2013; Ralph & Dettinger,  
70 2011; Ralph et al., 2006). Periods without regular precipitation will require water management  
71 strategies to adapt to ensure demands are met. Similarly, risk management plans and/or  
72 infrastructure for floods, landslides, and other water surplus associated hazards (such as dam  
73 failure) may also require reconsideration. This will be especially true if periods of precipitation,  
74 including those associated with atmospheric rivers, become more extreme, variable, and occur  
75 over a shorter window of time (Swain et al., 2018; Gershunov et al., 2019; Huang et al., 2020;  
76 Rhoades et al., 2020b; Rhoades et al., 2021). Changes in water availability due to climate  
77 “whiplash” will also have important ramifications for water resource management (Wang et al.,  
78 2017; Swain et al., 2018) and significantly increase annual flood damages based on the level of  
79 global warming that occurs (Rhoades et al., 2021). For example, in just the last two decades,  
80 California has experienced the most severe drought in the last 1200 years (Griffin & Anchukaitis,  
81 2014) followed by the wettest year on record (Di Liberto, 2017; SCRIPPS, 2017). These changes

82 in meteorological patterns may become the “new normal”, raising several outstanding questions  
83 related to how these changes in climate will impact the integrated hydrologic cycle, and  
84 subsequently water resource availability for humans and ecosystems.

85 To project how changes in climate will impact watershed behavior, high-resolution,  
86 physics-based models are one of the most promising ways to simulate system dynamics accurately,  
87 particularly those that are non-linear, and constitute a better way to analyze a no-analog future than  
88 the models used in the previous works. Previous studies analyzed future hydrologic conditions in  
89 California but relied on models that do not 1) account for the interactions, feedbacks, and  
90 movements of water from the lower atmosphere to the subsurface; 2) represent groundwater  
91 dynamics and lateral flow; 3) incorporate physics-based high-resolution climate models and/or 4)  
92 hydrologic models (e.g., Berghuijs et al., (2014); Gleick, (1987); He et al., (2019); Maurer, (2007);  
93 Safeeq et al., (2014); Son & Tague, (2019); Vicuna & Dracup, (2007); Vicuna et al., (2007)).  
94 Considerations of coupled interactions that explicitly account for groundwater connections are  
95 important (Condon et al., 2020, 2013; Maxwell and Condon, 2016), especially given groundwater  
96 is the largest reservoir in the terrestrial hydrologic budget and integral to water resource  
97 availability. Also, previous studies have focused on the mid-century period (e.g. Maurer & Duffy,  
98 2005; Son & Tague, 2019), which may indicate a more muted signal in hydrologic impacts than at  
99 EoC. Understanding these impacts is essential because long-term climate projections show that  
100 extremes will be more frequent and significant by the EoC (Cayan et al., 2008).

101 In this work, we assess the impacts of EoC extremely dry and intensely wet conditions on  
102 the hydrodynamics of a Californian watershed that contains one of the last naturally flowing rivers  
103 in the state. This allows us to investigate the impacts of climate change without the complexity of  
104 active water management, and thus to set the context for water management decisions. We

105 specifically investigate how the water and energy balance respond to climate extremes under  
106 climate change, and how those changes propagate to alter the spatiotemporal distribution of water  
107 in different hydrologic compartments of the watershed. We focus our investigation on the changes  
108 in groundwater and surface water storages. The balance of these two natural reservoirs, and their  
109 relationship in response to changes in snowpack reservoir changes, is important for water  
110 management decision making. We aim to 1) strengthen our physics-based understanding of the  
111 main hydrologic processes controlling changes in water storages under a changing climate, 2)  
112 quantify the magnitude and timing of these shifts in storage, and 3) identify the areas that are most  
113 vulnerable to change.

114 To do so, we utilize a novel combination of cutting-edge climate and hydrologic model  
115 simulations. We use an integrated hydrologic model (ParFlow-CLM; Maxwell & Miller, 2005),  
116 which solves the water-energy balance across the Earth's critical zone. When projecting  
117 hydrologic flows, ParFlow-CLM's explicit inclusion of three-dimensional groundwater flow is  
118 important given its demonstrated role in impacting land surface processes like evapotranspiration  
119 (Maxwell & Condon, 2016). We drive Parflow-CLM with climate forcing from a physics-based,  
120 variable-resolution enabled global climate model (the Variable Resolution enabled Community  
121 Earth System Model, VR-CESM; Zarzycki et al., 2014) that dynamically couples multi-scale  
122 interactions within the atmosphere-ocean-land system. This novel pairing of models allows for  
123 several key considerations not present in other methods. Our approach represents both dynamical  
124 and thermodynamic atmospheric response to climate change across scales, different from "pseudo-  
125 global warming" and "statistical delta" approaches used in many hydrologic modeling studies  
126 (e.g., Foster et al., 2020; Rasmussen et al., 2011). While these approaches are useful to isolate the  
127 impact of a given perturbation and/or variable, expected changes in climate will involve the co-

128 evolution of many processes, and may therefore not account for compensating factors. The  
129 interaction between dynamical and thermodynamic responses has important, and sometimes,  
130 offsetting effects on features such as atmospheric rivers. For example, Payne et al. (2020) show  
131 that the thermodynamic response to climate change enhances atmospheric river characteristics  
132 (e.g., Clausius-Clapeyron relationship), whereas the dynamical response diminishes atmospheric  
133 river characteristics (e.g., changes in the jet stream and storm track landfall location). Therefore,  
134 VR-CESM may simulate a more inclusive hydroclimatic response to climate change in the western  
135 United States at a resolution that is at the cutting-edge of today's global climate modeling  
136 capabilities for decadal-to-centennial length simulations (Haarsma et al., 2016).

137 We perform these couplings on spatial and temporal scales relevant for atmosphere-to-  
138 land, and land-to-subsurface interactions, an important consideration, given the recent work  
139 showing the importance of meteorological forcing resolution in representing the hydrologic cycle  
140 (Kampanhout et al., 2019; Maina et al., 2020b; Rhoades et al., 2016; Rhoades, Ullrich, Zarzycki,  
141 et al., 2018c; Wu et al., 2017). Climate conditions for EoC (2070-2100) and a 30-year historical  
142 period (1985-2015) are simulated to identify the median, wettest, and driest water year (WY) in  
143 each. We then simulate the subsequent watershed hydrology of each year using ParFlow-CLM  
144 forced with those meteorological conditions.

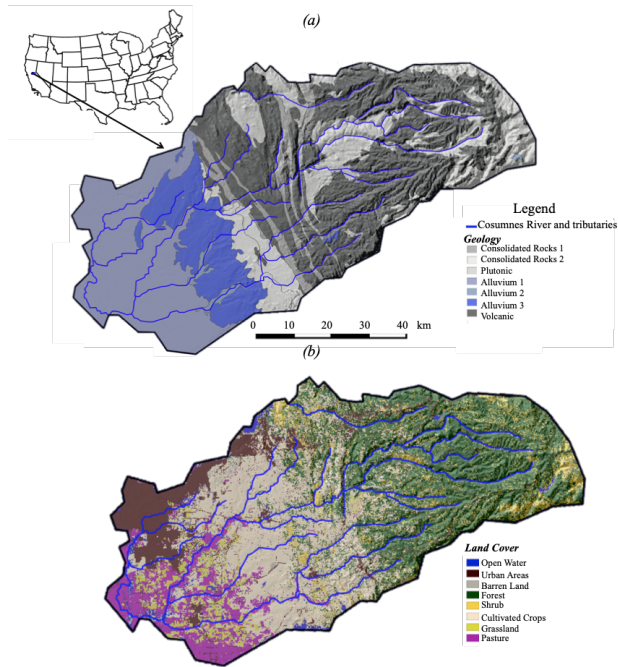
145

#### 146 **1. The Cosumnes watershed**

147 The Cosumnes River is one of the last rivers in the western United States without a major  
148 dam, offering a rare opportunity to isolate the impacts of a changing climate on the hydrodynamics  
149 without reservoir management consideration (Maina et al., 2020a; Maina and Siirila-Woodburn,  
150 2020). The watershed spans the Central Valley-Sierra Nevada interface and therefore represents

151 important aspects of the large-scale hydrology patterns of the state, namely the assessment of  
152 interactions between changes in precipitation, snowpack, streamflow, and groundwater across  
153 elevation and geologic gradients. Located in Northern California, USA, the Cosumnes watershed  
154 is approximately 7,000 km<sup>2</sup> in size (Figure 1) and is between the American and the Mokelumne  
155 rivers. Its geology ranges from low-permeability rocks typical of the Sierra Nevada landscape  
156 (volcanic and plutonic) to the porous and permeable alluvial depositions of the Central Valley  
157 aquifers. These are separated by very low-permeability marine sediments. The watershed  
158 topography includes a range of landscapes typical of the region (e.g. varying from flat agricultural  
159 land, rolling foothills, and steep mountainous hillsides), and elevation varies from approximately  
160 2500 m in the upper watershed to sea level in the Central Valley (Figure 1). The Sierra Nevada  
161 mountains are characterized by evergreen forest while the Central Valley hosts an intensive  
162 agricultural region including crops such as alfalfa, vineyards, as well as pastureland. Like other  
163 Californian watersheds, the climate in the Cosumnes is Mediterranean consisting of wet and cold  
164 winters (with a watershed average temperature equal to 0°C) and hot and dry summers (with  
165 watershed average temperature reaching 25°C) (Cosgrove et al., 2003).





166

167 Figure 1: The Cosumnes Watershed (a) location and geology (Jennings et al., 1977), the alluvium  
 168 in blue corresponds to the Central Valley aquifers whereas the consolidated rocks in gray  
 169 correspond to the Sierra Nevada and cross-cutting marine sediments, and (b) land cover (Homer  
 170 et al., 2015).

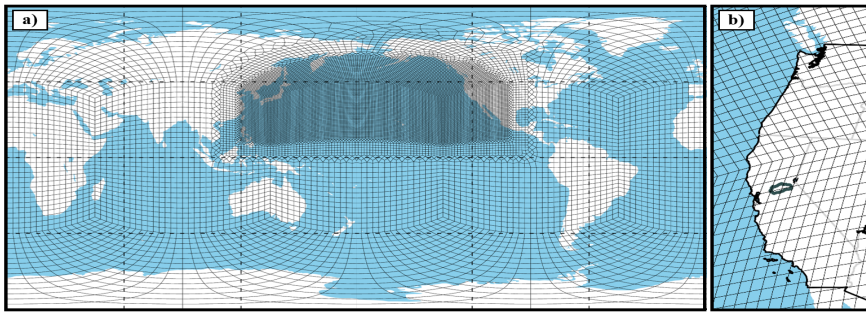
171

## 172 2. Experimental Design

### 173 2.1. Variable Resolution Community Earth System Model (VR-CESM)

174 Historical and EoC meteorological forcings are obtained from a simulation using the VR-  
 175 CESM at a regionally refined resolution of 28 km over the Northern Pacific Ocean through the  
 176 western United States, including the Cosumnes watershed and a global resolution of 111 km

177 (Figure 2). CESM has been jointly developed by NCAR (National Center for Atmospheric  
178 Research) and the DOE (U.S. Department of Energy) and simulates a continuum of Earth system  
179 processes including the atmosphere, land surface, land ice, ocean, ocean waves, and sea ice and  
180 the interactions between them (Collins et al., 2006; Gent et al., 2011; Hurrell et al., 2013). VR-  
181 CESM is a novel tool to perform dynamical downscaling as it allows for the interactions between  
182 the major components of the global climate system (e.g., atmosphere, cryosphere, land surface,  
183 and ocean) while allowing for regional-scale phenomena to emerge where regional refinement is  
184 applied, all within a single model (Huang et al., 2016; Rhoades et al., 2016; Rhoades, Ullrich, &  
185 Zarzycki, 2018b; Rhoades, Ullrich, Zarzycki, et al., 2018c).



186  
187 Figure 2: Variable Resolution Community Earth System Model (VR CESM) grid for (a) globe and  
188 (b) coastal western US with the Cosumnes watershed overlaid in dark gray.

189  
190 The atmospheric model used for these simulations is the Community Atmosphere Model  
191 (CAM) version 5.4 with the spectral element dynamical core, with an atmospheric dynamics time  
192 step of 75 seconds, an atmospheric physics time step of 450 seconds, a prognostic treatment of  
193 rainfall and snowfall in the microphysics scheme (Gettelman and Morrison, 2015) and run under  
194 Atmosphere Model Intercomparison Project (AMIP) protocols (Gates, 1992). Under the AMIP  
195 protocols, the atmosphere and land-surface components of the Earth system model are coupled

196 and periodically bounded by monthly observed sea-surface temperatures and sea-ice extents.  
197 Although this configuration does not exactly recreate historical water years and events, it is  
198 expected to reasonably simulate the distribution of water year types. Also, it should be noted that  
199 the model only projects future conditions, within the envelope of plausible future conditions of the  
200 RCP8.5 scenario and its assumptions of greenhouse gas emissions, sea-surface temperatures, and  
201 sea ice extents and would not be expected to exactly forecast individual water years. Simulations  
202 with VR-CESM are performed for 30-year periods based on the climates from a historical period  
203 (1985-2015) and an EoC period (2070-2100). EoC simulations, analogous to Rhoades, Ullrich, &  
204 Zarzycki, 2018, are bounded by estimates of future changes in ocean conditions derived from a  
205 fully-coupled bias-corrected CESM simulation (assuming historical ocean simulation biases will  
206 be similar in the future simulation) and forced by greenhouse gases and aerosol concentrations  
207 assumed in the RCP8.5 emissions scenario. Historical VR-CESM outputs have been compared  
208 with reanalyses and future VR-CESM outputs have been analyzed for shifts in  
209 hydrometeorological extremes in further detail in Rhoades et al., 2020 a,b. To couple the outputs  
210 with ParFlow-CLM, we regrid the unstructured 28km VR-CESM data over the Cosumnes  
211 watershed using bilinear interpolation in the Earth System Modeling Framework (Jones, 1999) to  
212 a final resolution of approximately 11 km (i.e., 57 grids over the Cosumnes watershed). Notably,  
213 each of the spectral elements in the VR-CESM grid, shown in Figure 1, has a 4x4 set of Gauss–  
214 Lobatto–Legendre (GLL) quadrature nodes where equations of the atmospheric model are solved  
215 (Herrington et al., 2019). Therefore, the actual resolution at which the atmospheric dynamics and  
216 physics are solved in VR-CESM are at higher-resolution (~28km) than is shown in Figure 1,  
217 making these some of the highest resolution global Earth system model simulations over California  
218 to date (Haarsma et al., 2016).

219 To identify if VR-CESM is fit for purpose to simulate historical dry, median, and wet WYs,  
220 and inform potential biases in future projections (over California and, more specifically, the  
221 Cosumnes watershed), we first conduct a model comparison to a widely used observational  
222 product, the Parameter-elevation Relationships on Independent Slopes Model (PRISM; Daly et al.,  
223 2008) at 4 km resolution analogous to Rhoades et al., (2020a). However, in this study, we focus  
224 our assessment of VR-CESM fidelity over California and the Cosumnes watershed. PRISM  
225 provides daily precipitation, mean dewpoint temperature and maximum and minimum surface  
226 temperature, and vapor pressure. PRISM precipitation and temperature data spanning 1981-2019  
227 are compared with the VR-CESM 1985-2015 simulations. We note that a mismatch in the time  
228 period (1981-2019 versus 1985-2015) is deliberate. As stated previously, VR-CESM is simulated  
229 under AMIP-protocols (bounded by monthly observed sea-surface temperatures and sea-ice  
230 extents), and therefore we do not expect VR-CESM to exactly recreate past historical WYs.  
231 However, we do expect that our 30-year simulation can reasonably recreate the range of WY types  
232 over California and the Cosumnes, which is why we utilize the broader range of PRISM WYs that  
233 are available. For this comparison, we regrid the unstructured VR-CESM data to 4km resolution  
234 (the native resolution of PRISM) using the Earth System Modeling Framework (ESMF) Offline  
235 Re-gridding Weight Generator in the NCAR Command Language (NCL, 2021).

236 The comparison (discussed in appendix A) indicates that VR-CESM reasonably reproduces  
237 the historical WY conditions (i.e., interannual range of PRISM precipitation largely overlaps with  
238 the range of model bias simulated by VR-CESM). VR-CESM generally simulates a wetter  
239 historical period over the Cosumnes (range of bias of 1330 mm) relative to PRISM (range of  
240 interannual variability of 1320 mm). Basin-average minimum (421 mm) and maximum (1740 mm)  
241 WY accumulated precipitation are slightly larger than those of PRISM. Of relevance to this study,

242 PRISM has shown notable uncertainties in the Sierra Nevada. Lundquist et al., 2015 showed that  
 243 an underrepresentation of the most extreme storm total precipitation in the Sierra Nevada can result  
 244 in an upper-bound uncertainty of 20% in WY accumulated precipitation in PRISM. Therefore, the  
 245 wettest WY simulated by VR-CESM is well within the 20% uncertainty range of PRISM's wettest  
 246 WY (1580 ± 316 mm). Further, differences in basin-average WY accumulated precipitation  
 247 between VR-CESM and PRISM are non-significant using a t-test and assuming a p-value < 0.05.  
 248 As discussed in further detail below, we posit that atmospheric river-related precipitation is likely  
 249 the driver of the wet bias mismatch with PRISM. However, we also note that the uncertainty  
 250 bounds of the PRISM product WY precipitation totals in the Sierra Nevada are estimated to be  
 251 upwards of ~20% too dry (e.g., Lundquist et al., 2015), particularly for extreme precipitation  
 252 events such as atmospheric rivers and in mountainous terrain.

253

## 254 **2.2. Integrated Hydrologic Model: ParFlow-CLM**

255 The integrated hydrologic model ParFlow-CLM (Kollet & Maxwell, 2006; Maxwell, 2013;  
 256 Maxwell & Miller, 2005) solves the transfer and interactions of water and energy from the  
 257 subsurface to the lower atmosphere including groundwater dynamics, streamflow, infiltration,  
 258 recharge, evapotranspiration, and snow dynamics. The model describes 3D groundwater flow in  
 259 variably saturated media with the Richards equation (equation 1, Richards, 1931) and 2D overland  
 260 flow with the kinematic wave equation (equation 2).

$$261 \quad S_S S_W(\psi_P) \frac{\partial \psi_P}{\partial t} + \phi \frac{\partial S_W(\psi_P)}{\partial t} = \nabla \cdot [K(x) k_r(\psi_P) \nabla (\psi_P - z)] + q_s \quad (1)$$

262 Where is  $S_S$  the specific storage ( $L^{-1}$ ),  $S_W(\psi_P)$  is the degree of saturation (-) associated  
 263 with the subsurface pressure head  $\psi_P$  (L),  $t$  is the time (T),  $\phi$  is the porosity (-),  $k_r$  is the relative

264 permeability (-),  $z$  is the depth,  $q_s$  is the source/sink term ( $T^{-1}$ ) and  $K(x)$  is the saturated hydraulic  
265 conductivity ( $L T^{-1}$ ).

266 ParFlow solves the mixed form of the Richards equation which has the advantage of  
267 conserving the mass (Celia et al., 1990).

268 The kinematic wave equation is used to describe surface flow in two dimensions is defined  
269 as:

$$270 \quad -k(x)k_r(\psi_0)\nabla(\psi_0 - z) = \frac{\partial\|\psi_0,0\|}{\partial t} - \nabla \cdot v\|\psi_0,0\| - q_r(x) \quad (2)$$

271 Where  $\psi_0$  is the ponding depth,  $\|\psi_0,0\|$  indicates the greater term between  $\psi_0$  and 0,  $v$  is  
272 the depth averaged velocity vector of surface runoff ( $L T^{-1}$ ),  $q_r$  is a source/sink term representing  
273 rainfall and evaporative fluxes ( $L T^{-1}$ ).

274 Surface water velocity at the surface in  $x$  and  $y$  directions,  $(v_x)$  and  $(v_y)$  respectively, is  
275 computed using the following set of equations:

$$276 \quad v_x = \frac{\sqrt{S_{f,x}}}{m} \psi_0^{\frac{2}{3}} \quad \text{and} \quad v_y = \frac{\sqrt{S_{f,y}}}{m} \psi_0^{\frac{2}{3}} \quad (3)$$

277 Where  $S_{f,x}$  and  $S_{f,y}$  friction slopes along  $x$  and  $y$  respectively and  $m$  is the manning coefficient.

278 ParFlow employs a cell-centered finite difference scheme along with an implicit backward Euler  
279 scheme and the Newton Krylow linearization method to solve these nonlinear equations. The  
280 computational grid follows the terrain to mimic the slope of the domain (Maxwell, 2013).

281 ParFlow has many advantages in comparisons to other hydrologic models. Compared to  
282 other hydrologic models (MODFLOW (Harbaugh, 2005), FEFLOW (Trefry and Muffels, 2007),  
283 SWAT (Soil and Water Assessment Tool) (Neitsch et al., 2000), SAC-MA (Sacramento Soil  
284 Moisture Accounting Model)), ParFlow has the advantages of accounting for land surface  
285 processes such as snow dynamics and evapotranspiration and their interactions with the subsurface  
286 which are crucial for studying the hydrology of California. ParFlow also solved the subsurface

287 flow by accounting for variably saturated conditions, an important feature for calculating  
288 groundwater recharge and the connection between the groundwater and the land surface processes,  
289 which is not the case for the aforementioned models. While some hydrologic models have a better  
290 representation of the land surface processes (Noah-MP (Niu et al., 2011), VIC (Variable  
291 Infiltration Capacity Model Macroscale Hydrologic Model) (Liang et al., 1994)), these models do  
292 not have a detailed representation of the subsurface flows. Because the surface flow is important  
293 in the region and it establishes the connection between the headwaters and the valleys, its good  
294 representation is essential for projecting changes in hydrology. Compared to other integrated  
295 hydrologic models (CATHY (Catchment Hydrology) (Bixio et al., 2002), MIKE-SHE (Abbott et  
296 al., 1986)), ParFlow has the advantages of solving a two-dimensional kinematic flow equation that  
297 is fully coupled to the Richards equation.

298 ParFlow is coupled to the Community Land Model (CLM) to solve the surface energy and  
299 water balance, which enables interactions between the land surface and the lower atmosphere and  
300 the calculation of key land surface processes governing the system hydrodynamics such as  
301 evapotranspiration, infiltration, and snow dynamics. CLM models the thermal processes by closing  
302 the energy balance at the land surface given by:

303 
$$R_n(\theta) = LE(\theta) + H(\theta) + G(\theta) \quad (4)$$

304 Where  $\theta = \phi S_w$  is the soil moisture,  $R_n$  is the net radiation at the land surface (E/LT) a  
305 balance between the shortwave (also called solar) and longwave radiation,  $LE$  is the latent heat  
306 flux (E/LT) which captures the energy required to change the phase of water to or from vapor,  $H$   
307 is the sensible heat flux (E/LT) and  $G$  is the ground heat flux (E/LT).

308 More information about the coupling between ParFlow and CLM can be found in Maxwell  
309 & Miller, (2005). CLM uses the following outputs of the VR-CESM model at 3-hourly resolution

310 to solve the energy balance at the land surface: precipitation, air temperature, specific humidity,  
311 atmospheric pressure, north/south and east/west wind speed, and shortwave and longwave wave  
312 radiation.

313 We constructed a high-resolution model of the Cosumnes watershed with a horizontal  
314 discretization of 200 m and vertical discretization that varies from 10 cm at the land surface to 30  
315 m at the bottom of the domain. The model has 8 layers, the first 4 layers represent the soil layers  
316 and the other four the deeper subsurface. The total thickness of the domain is 80 m to ensure  
317 appropriate representation of water table dynamics. Observed water table depths (as measured at  
318 several wells located in the Central Valley portion of the domain) vary between approximately 50  
319 m and the land surface through a multi-year time period (Maina et al., 2020a). Therefore, to be  
320 conservative for imposing the lower boundary layer, anything below 80 m is expected to remain  
321 fully saturated. The resulting model comprises approximately 1.4 million active cells and was  
322 solved using 320 cores in a high-performance computing environment. The Cosumnes watershed  
323 is bounded by the American and Mokelumne rivers. We, therefore, impose weekly varying values  
324 of Dirichlet boundary conditions along these borders to reflect the observed changes of river  
325 stages. The eastern part of the watershed corresponding to the upper limit in the Sierra Nevada is  
326 modeled as a no-flow (i.e., Neumann) boundary condition. Hydrodynamic parameters required to  
327 solve the surface and subsurface flows (e.g., hydraulic conductivity, specific storage, porosity, and  
328 van Genuchten parameters) are derived from a regional geological map (Geologic Map of  
329 California, 2015; Jennings et al., 1977) and a literature review of previous studies (Faunt et al.,  
330 2010; Faunt and Geological Survey (U.S.), 2009; Gilbert and Maxwell, 2017; Welch and Allen,  
331 2014). We use the 2011 National Land Cover Database (NLCD) map (Homer et al., 2015) to  
332 define land use and land cover required by CLM. We further delineate specific croplands (notably



333 alfalfa, vineyards, and pasture) in the Central Valley by using the agricultural maps provided by  
334 the National Agricultural Statistics Service (NASS) of the US Department of  
335 Agriculture's (USDA) Cropland Data Layer (CDL) (Boryan et al., 2011). Vegetation parameters  
336 are defined by the International Geosphere-Biosphere Programme (IGBP) database (IGBP, 2018).  
337 A complete description of the model parameterization can be found in appendix B and more details  
338 in Maina et al. (2020a). The model has been extensively calibrated and validated using various  
339 datasets, including remotely sensed data and ground measurements, which are however very sparse  
340 in the area. Model validation which consists in comparing both surface and subsurface  
341 hydrodynamics (groundwater and river stages) and land surface processes was performed over a  
342 period of three years that includes extremely dry and wet water years (Appendix C). We  
343 specifically compared simulated and measured river stages at three stations located in the Sierra  
344 Nevada headwater, foothill, and the Central Valley. The annual averages absolute differences  
345 between measurements and simulations were between 0.4 and 0.8 m. We selected four wells in the  
346 Cosumnes watershed based on their availability of data to compare measured and simulated  
347 groundwater levels. These wells are sparsely distributed in the Central Valley. The absolute  
348 differences between observed and simulated groundwater levels vary between 0.47 to 3.73 m. The  
349 highest absolute differences were attributed to the lack of best estimations of groundwater pumping  
350 rates in the region. Nonetheless, the reasonable agreement between observations and simulated  
351 variables over a period that includes both extremely dry and intensely wet conditions has allowed  
352 us to conclude that the model can capture these extreme dynamics. We rely on remote sensing  
353 data to assess the ability of our model to simulate key land surface processes (evapotranspiration  
354 *ET*, soil moisture, and snow water equivalent *SWE*). We compared the simulated *SWE* to SNODAS  
355 (The National Weather Service's Snow Data Assimilation, National Operational Hydrologic

356 Remote Sensing Center, 2004) and a *SWE* reanalysis by Bair et al., (2016). Our comparisons  
357 indicated that the absolute differences between our *SWE* values and these data were equal to 3 mm  
358 on average. Moreover, the simulated key parameters controlling the snow dynamics such as peak  
359 snow and timing of snow ablation were also in agreement with remotely sensed data for both dry  
360 and wet years (Appendix C). Absolute differences between the simulated *ET* and the remotely  
361 sensed *ET* from METRIC (Mapping Evapotranspiration at High Resolution with Internalized  
362 Calibration, Allen et al., 2007) were equal to 0.036 mm/s while the differences between the  
363 simulated soil moisture and the SMAP (Soil Moisture Active Passive, SMAP, 2015) soil moisture  
364 were 0.2. More details about model calibration and validation can be found in Appendix C and  
365 previous publications (Maina et al., 2020a, Maina et al., 2020b; Maina and Siirila-Woodburn,  
366 2020c). The model has also been successfully used in recent investigations of post-wildfire and  
367 climate extremes hydrologic conditions and to assess the role of meteorological forcing scale on  
368 simulated watershed dynamics (Maina et al., 2020a, b; Maina and Siirila-Woodburn, 2020c).  
369 Initial conditions for pressure-head were obtained by a spin-up procedure using the forcing of the  
370 historical median WY. We recursively simulated the historical median WY forcing until the  
371 differences of storage at the end of the WY were less than 1%, indicating convergence. This  
372 pressure head field is then used as the initial condition for each of the five WYs of interest (i.e.,  
373 the EoC wet, EoC dry, historic wet, historic dry, EoC median). Though we acknowledge land  
374 cover alterations are expected to occur by the EoC (either naturally or anthropogenically), in this  
375 work we assume that the vegetation remains constant for both historical and EoC simulations for  
376 simplicity. Although outside of the scope of this work, future studies will investigate the impacts  
377 of an evolved land use/land cover, vegetation physiology, and resilience strategies to manage water  
378 resources. Further, while the Central Valley of California hosts intensive agriculture that is reliant

379 on groundwater pumping for irrigation, we didn't incorporate pumping and irrigation in our model  
380 configuration. We did this with the assumption that groundwater pumping rates may substantially  
381 change in the future due to new demands, policies, regulations, and changes in land cover and land  
382 use and aim to provide an estimate of the natural hydrologic system response to climate change.

383

### 384 **2.3. Analysis of EoC hydrodynamics**

385 To investigate how the EoC climate extremes affect water storages, we investigate five  
386 hydrologic variables: *SWE*, *ET*, Pressure-head ( $\psi$ ) distributions, and surface and subsurface water  
387 storage. Total groundwater (GW) storage is given by:

$$388 \quad Storage_{GW} = \sum_{i=1}^{n_{GW}} \Delta x_i \times \Delta y_i \times \Delta z_i \times \psi_i \times \left( \frac{S_{s_i}}{\phi_i} \right) \quad (5)$$

389 where  $n_{GW}$  is the total number of subsurface saturated cells (-),  $\Delta x_i$  and  $\Delta y_i$  are cell discretizations  
390 along the x and y directions (L),  $\Delta z_i$  is the discretization along the vertical direction the cell (L),  
391  $S_{s_i}$  is the specific storage associated with cell  $i$ ,  $\psi_i$  the pressure-head, and  $\phi_i$  is the porosity.

392 Total surface water (SW) storage which accounts for any water located at the land surface  
393 (i.e., any cell of the model with a pressure-head greater than 0) and includes river water or overland  
394 flow is calculated via:

$$395 \quad Storage_{SW} = \sum_{i=1}^{n_{SW}} \Delta x_i \times \Delta y_i \times \psi_i \quad (6)$$

396 where  $n_{SW}$  is the total number of cells with surface water i.e., with surface  $\psi$  greater than 0 (-),  
397 and  $i$  indicates the cell.

398 We compare each EoC WY simulation to its corresponding historical WY counterpart and  
399 both the historical and EoC medians. This allows us to assess how EoC extremes change relative  
400 to what is currently considered an extreme condition as well as to “normal” in the relevant time.  
401 Comparisons are shown as a percent change (*PC*) calculated using:

402 
$$PC_{i,t} = \frac{X_{projection_{i,t}} - X_{baseline_{i,t}}}{X_{baseline_{i,t}}} \times 100 \quad (3)$$

403 where  $X$  is the model output ( $ET$ ,  $SWE$ , or  $\psi$ ) at a given point in space ( $i$ ) at a time ( $t$ ), *baseline* is  
404 the selected simulation (historical median, EoC median, or historical extreme), and *projection*  
405 represents the simulation obtained with the EoC extreme WYs (dry or wet).

406

### 407 **3. Results**

408 In this section, we present a subset of the outputs from VR-CESM (precipitation and  
409 temperature) to identify the extreme (dry and wet) and median WYs of interest. Changes in fluxes  
410 and storages over the course of each WY, as well as the spatial variability of these changes in two  
411 important periods of the WY (peak flow and baseflow) are also shown.

412

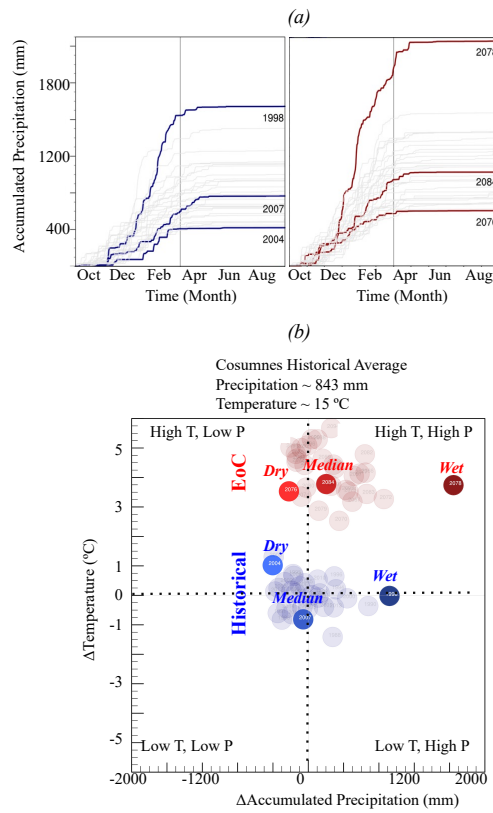
#### 413 **3.1. Selection of the median, dry, and wet WYs**

414 From the historical and EoC 30-year VR-CESM simulations we select the median, wettest,  
415 and driest WYs for comparison (see Figure 3a). Overall, the future WYs are ~30% wetter than the  
416 historical WYs (p-value ~0.006 for two-tailed t-test of equal average annual precipitation) in  
417 addition to being ~4.6°C warmer. Precipitation and temperature variances are mostly similar in the  
418 historical and EoC simulations, though EoC minimum temperature may be more variable (p-value  
419 ~0.059 for two-tailed f-test of equal variance in minimum temperature). On average the timing for  
420 the start, length, and end of precipitation is similar, though EoC precipitation may be less variable  
421 in its start time (p-value ~0.053 for f-test of equal variance in days to reach 5<sup>th</sup> percentile of annual  
422 precipitation). In the climate model, there are no clear trends between the precipitation timing  
423 metrics and total amount of precipitation.

424           The EoC median WY is much wetter than its historical counterpart, with about ~250 mm  
425 more precipitation that begins approximately 1 week earlier and ends approximately 2 weeks  
426 earlier in the year. The EoC wettest WY is much wetter than the historical wettest WY and is  
427 characterized by 42% more precipitation. This is consistent with Allan et al. (2020), who suggest  
428 a wetter future. The EoC wettest WY is 3.8°C warmer than the historical wettest WY and 4.6°C  
429 warmer than the historical median WY, as the historical median WY is one of the coolest years in  
430 the series. Precipitation occurs earlier in the EoC wet WY compared to the historical wet or median  
431 WYs, with the 5<sup>th</sup> percentile of precipitation reached 12 days earlier in the EoC wettest WY than  
432 either the wettest or median historical WYs. The duration of the EoC wettest WY precipitation  
433 season (146 days) is between the historical wettest WY (133 days) and the historical median WY  
434 (155 days).

435           The EoC dry WY is also much wetter than its historic counterpart; in fact, the EoC dry WY  
436 is wetter than the seven driest historical WYs of the 30-year historical ensemble. Simulation of 30  
437 random draws from two identical normal distributions, repeated 100,000 times, finds that the  
438 lowest value in one is higher than the seven lowest values in the other only ~1.1% of the time (p-  
439 value ~0.011). This statistical test reveals that this VR-CESM simulation suggests that future dry  
440 years will be somewhat wetter than historical dry years. The EoC dry WY is only ~2.5°C warmer  
441 than the historical dry WY. The divergence in temperature is smaller for the comparison of EoC  
442 and historical WYs of the dry extremes as opposed to the wet extremes because the historical dry  
443 WY is the second-warmest WY in the historical simulations, while the EoC dry WY is the third  
444 coolest in the EoC simulations. Precipitation in the EoC dry WY starts particularly early, with the  
445 5<sup>th</sup> percentile of annual precipitation reached by mid-October. This is much earlier than either the  
446 dry or median historical WYs, which don't reach that percentile of precipitation until mid-to-late

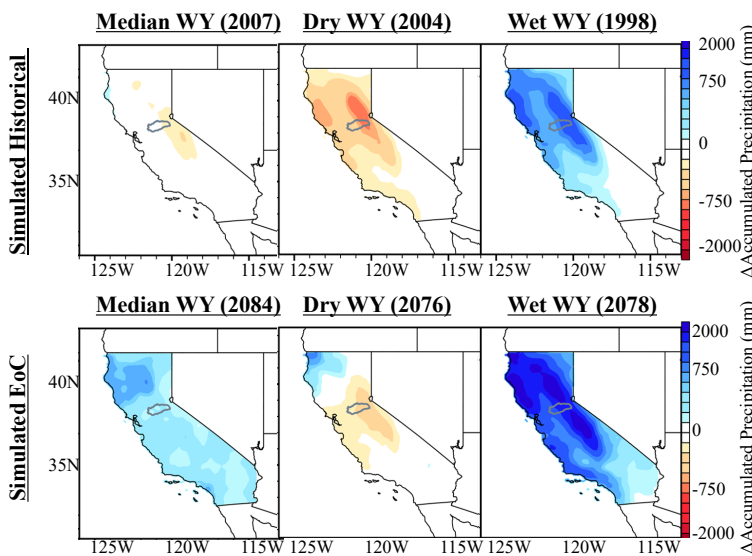
447 November. The historical dry WY also has a particularly short precipitation duration of only 97  
 448 days, while the EoC dry WY has a 163-day precipitation duration, more similar to the median  
 449 historical WY duration of 155 days.



450 Figure 3: (a) VR-CESM accumulated total precipitation for the historical and End of Century  
 451 (EoC) simulations, and (b) quadrants for differences between each individual water year (WY)  
 452 and the historical average temperature and accumulated precipitation in the Cosumnes watershed.  
 453 The historical and EoC dry, median and wet WYs are indicated in blue and red, respectively.  
 454  
 455

456 Figure 4 shows the spatial distribution of accumulated precipitation anomalies across  
457 California. These anomalies are computed for each of the six identified WYs relative to the  
458 climatological average (the 30-year historical mean). These spatial plots provide context for the  
459 changes modeled in the Cosumnes watershed relative to broader precipitation changes California-  
460 wide. As in the Cosumnes, California-wide EoC dry, median, and wet WYs are all characterized  
461 by higher precipitation totals than their historical counterparts. Importantly, the EoC wet WY is a  
462 true outlier not only in the Cosumnes but across California too. California lies at an important  
463 large-scale circulation transition, namely semi-permanent high-pressure systems associated with  
464 the Hadley circulation. Therefore, how climate change alters the atmospheric dynamics over  
465 California, or more specifically how far northward storm-tracks may shift, remains uncertain and  
466 depends on climate model choice. This has led to papers that claim the future of California will be  
467 wet across a range of climate models (e.g., Neelin et al, 2013; Swain et al., 2013; Gershunov et al.,  
468 2019; Rhoades et al., 2020b; Persad et al., 2020) and, for select climate models, that it could be  
469 drier. Notably, these studies highlight an asymmetric response in the frequency of wet versus dry  
470 WYs (i.e., anomalously wet WYs increase in frequency much more in the future than anomalously  
471 dry WYs). Many of the aforementioned studies also highlight that in anomalously wet WYs  
472 extreme precipitation events (e.g., atmospheric rivers) will occur with greater intensity and  
473 frequency and largely drive changes in WY precipitation totals (which is shown in our VR-CESM  
474 simulations for California in more detail in Rhoades et al., 2020b). Given these complexities and  
475 others such as consideration for how dynamical and thermodynamical effects of climate change  
476 may interact with one another to offset or amplify extreme precipitation events (Payne et al., 2020),  
477 the hypothesis that global warming will result in a climate where the “wet gets wetter and dry gets  
478 drier” may be too simplistic of an assumption for California. Rhoades et al., (2020b) shows

479 quantitatively that the increases in precipitation observed in the VR-CESM outputs are due to a  
 480 greater number of intense atmospheric river events that occur more regularly back-to-back, which  
 481 was recently corroborated by Rhoades et al. (2021) using uniform-high-resolution CESM  
 482 simulations at different warming scenarios, and that atmospheric river precipitation totals increase  
 483 at a much larger rate (+53%/K) than non-AR precipitation totals (+1.4%/K), which agrees with  
 484 findings made in other studies such as Gershunov et al. (2019).



485  
 486 Figure 4: Precipitation spatial distributions of the dry, median, and wet water years (WY) for the  
 487 30-year historical and EoC simulations relative to the climatological average (derived from the 30-  
 488 year historical mean)

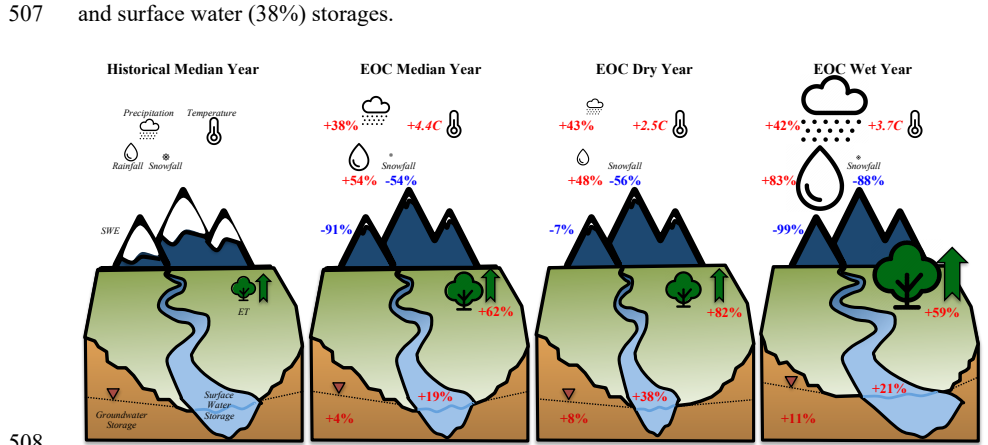
489

### 490 3.2. Changes in annual watershed-integrated fluxes and storages

491 Figure 5 illustrates the annual changes in the integrated hydrologic budget of the Cosumnes  
 492 watershed for the EoC WYs (i.e., median, dry, and wet) compared to the historical median WY.



493 The EoC median WY compared to the historical median WY has 38% more precipitation and the  
 494 temperature is 4.4°C higher. Further, the precipitation phase also shifts with an increase in rainfall  
 495 (54%) and a decrease in snowfall (-54%). This results in a significant decrease in *SWE* (-91%)  
 496 which is consistent with many other studies that have shown that increased temperatures due to  
 497 climate change will lead to low-to-no snow conditions (Berghuijs et al., 2014; Cayan et al., 2008;  
 498 Mote et al., 2005; Rhoades et al., 2018 a,b; Son & Tague, 2019). The increase in temperature and  
 499 precipitation results in an increase in *ET* (62%), consistent with the findings of other recent studies  
 500 (e.g. McEvoy et al., 2020). Nevertheless, the larger amount of precipitation associated with the  
 501 EoC is enough to offset higher *ET* demand and recharge groundwater and surface water, which  
 502 experience an increase of 4% and 19% respectively. The EoC wet WY has similar changes as the  
 503 EoC median WY when compared to the historical wet WY yet the magnitude of the increase in  
 504 surface (21%), and groundwater (11%) storages are higher due to more precipitation and higher  
 505 temperatures. The dry EoC WY is also characterized by higher precipitation (43%, the largest  
 506 increase) than its historical counterpart, this results in large increases in total groundwater (8%)  
 507 and surface water (38%) storages.

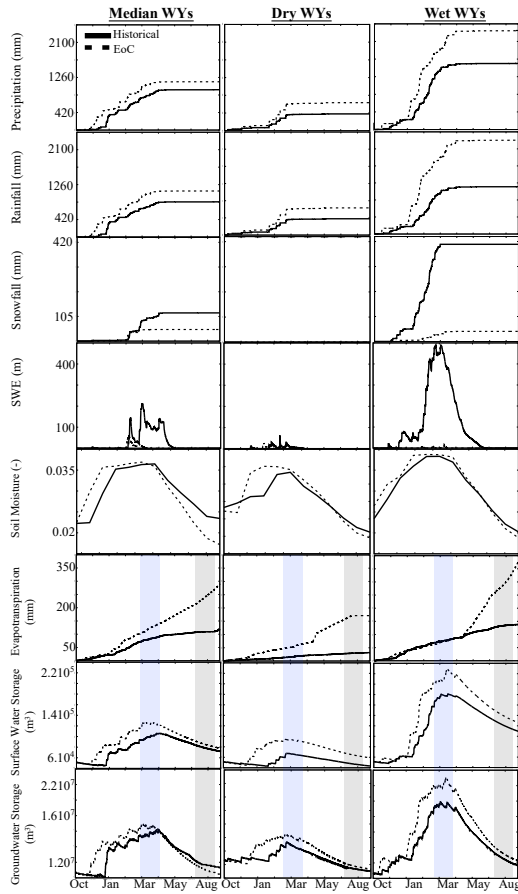


509 Figure 5: Annual percent changes in precipitation, rainfall, snowfall, temperature, *SWE*, *ET*,  
510 surface water, and groundwater storages in the EoC water years (WY) (i.e median, dry, and wet)  
511 at the watershed scale relative to their historical counterparts. Info-graphic size scaled to EoC  
512 conditions.

513

### 514 **3.3. Temporal variation of watershed-integrated fluxes and storages**

515 Understanding the annual changes at the watershed scale is important to broadly  
516 understand changes in the water budget in response to future climate extremes. However, a deeper  
517 understanding of the processes that drive these changes and the interactions from atmosphere-  
518 through-bedrock requires an analysis of their spatiotemporal variations as well. Figure 6 shows  
519 the temporal variations of each of the historical and EoC WY's integrated hydrologic budgets  
520 grouped by WY type (columns), with a top-down sequencing of hydrologic variables of interest in  
521 order from the atmosphere through subsurface (rows). This organization allows for the  
522 investigation of propagating impacts to be directly compared in time. In this section, we discuss  
523 historical vs EoC changes observed in each of the WY types (i.e., median, dry, and wet). Each WY  
524 shows unique hydrodynamic behaviors and changes compared to the historical conditions. The  
525 median WY sheds light on how changes in the precipitation phase and increases in temperature  
526 and precipitation in the EoC will impact the hydrodynamics. The dry WYs allow comparing EoC  
527 and historical low-to-no snow conditions whereas assessing the hydrodynamics of the EoC wet  
528 WY provides a better understanding of how intense EoC precipitation along with the warm EoC  
529 climate will shape the hydrology.



530

531 Figure 6: Temporal variations of the total cumulative precipitation, rainfall, and snowfall at the  
 532 watershed scale, total *SWE* at the watershed scale, the average watershed values of soil moisture,  
 533 the cumulative watershed *ET*, and the total surface water, and groundwater storages at the  
 534 watershed scale associated with the six historical and EoC Water Years (WY). The blue area  
 535 indicates the selected peak flow period while the gray area corresponds to the selected baseflow  
 536 conditions for the spatial distribution analyses.

537

538

### 3.3.1. Median water years

539

540

541

542

543

544

545

546

547

548

549

550

551

552

553

554

555

556

557

558

559

As indicated in section 3.1, the EoC median WY has more precipitation than the historical median WY. The EoC precipitation comes mainly as rain due to the warmer temperatures of the EoC and includes virtually no snowfall from late winter to early spring. This precipitation phase-change combined with the earlier snowfall cessation date in the WY results in minimal and even non-existent *SWE* in the Cosumnes watershed for much of the WY, a significant change compared to historic conditions. EoC peak *SWE* occurs in February in contrast to the historical peak *SWE*, which occurs in April. Due to the watershed's relatively low elevation, snow accumulates only in the upper part of the Cosumnes watershed (~10% of the total watershed area). Only areas located in the highest elevations (> 2000 m), such as the eastern limit of the watershed, show any *SWE* in the EoC simulations whereas in the historical WYs we observed *SWE* as low as 1000 m.

The decrease in snow and the increase in rain along with an earlier onset of seasonal precipitation directly impacts soil moisture, which sees an early increase with a slightly higher peak than historical. As more water is available earlier in the EoC, the *ET* demand from increased temperatures is met until substantially higher summer temperatures increase *ET* at a much faster rate than the historical WY. The high EoC *ET* and the lack of snowmelt cause the soil to rapidly dry from late-spring through late-summer.

Because of the marked increase in total precipitation and shift from snow to rain in the EoC simulations, surface water storage generally increases throughout the WY. This is consistent with previous studies (Gleick, 1987; He et al., 2019; Maurer, 2007; Safeeq et al., 2014; Son & Tague, 2019; Vicuna & Dracup, 2007; Vicuna et al., 2007). Surface water storage increases in early November in the EoC simulations while in the historical simulations this increase occurs in

560 January. Similar to the earlier peak *SWE* and soil moisture, the peak surface water storage in the  
561 EoC is also earlier (January through February) compared to the historical period (March through  
562 April). This late-season surface water storage remains larger because the accumulated precipitation  
563 is large enough to overcome the increased *ET* in a warmer climate. Similar to surface water storage,  
564 groundwater storage increases earlier and peaks at a larger amount than the historical WY.  
565 However, in contrast to the surface water storage, the groundwater storage during baseflow  
566 conditions is lower in the median EoC compared to the median historical year. This decrease in  
567 groundwater during baseflow conditions is due to the lack of snowmelt and higher EoC *ET*. In late  
568 spring and summer in the EoC, groundwater keeps depleting through *ET* and is not recharged by  
569 snowmelt through surface and subsurface flows from the Sierra Nevada as in the historical period.  
570 This may indicate that compared to surface water storages, groundwater storage may be more  
571 sensitive to EoC hydroclimatic changes (which are multi-fold, and in this case include an increase  
572 in precipitation, a transition from snow to rain, and higher *ET*). One way to quantitatively measure  
573 this sensitivity is to compare the seasonal change in water storage between peak and baseflow  
574 conditions. Historically, changes between peak and baseflow conditions (i.e., the amount of water  
575 lost between peak and base flow) resulted in moderate seasonal changes in groundwater storage  
576 (30%) and surface water storage (32%). The EoC simulations reveal larger seasonal variation for  
577 groundwater and surface water storage (40% and 37% decreases, respectively). Groundwater in  
578 the Cosumnes Watershed is mainly recharged in the headwaters and stored in the Central Valley.  
579 Therefore, these Central Valley aquifers experience earlier and larger increases in storage which  
580 lead to more water available to *ET* and therefore aquifer depletion. A deeper understanding of this  
581 phenomenon requires an analysis of the spatial patterns of these changes which is performed later  
582 on in this study.

583

584

### 3.3.2. Dry water years

585

586

587

588

589

590

591

592

593

594

595

596

597

598

599

600

601

602

603

604

605

All EoC WYs are characterized by higher precipitation in the form of rainfall compared to their historical counterparts. The historical dry WY has ~43% less total precipitation than the EoC dry WY. However, we note that for the EoC dry WY the decrease in snowfall is less drastic than the median or wet EoC years. This is because the historically driest WY is significantly warmer than the historical average WY, and therefore already has a smaller snowpack, 94% lower than the historical median WY. The EoC dry WY *SWE* also accumulates two months earlier than the historical *SWE*. Because the differences in *SWE* between the dry WYs are smaller than the differences in *SWE* between the median WYs (7% versus 91%), we can deduce that the early and larger rise in soil moisture in the EoC dry WY is mostly due to an earlier and larger amount of rainfall. The higher soil moisture and EoC temperatures result in higher *ET* throughout the WY compared to the historical WY. This *ET* results in lower soil moisture by the end of the summer, similar to the median WY. In addition, surface water storage peaks earlier and at a larger amount compared to the historical WY. The surface water storage in the EoC remains higher throughout the WY compared to its historical counterpart despite this higher *ET* due to the low precipitation associated with the historical dry WY. We further note that the difference in surface water storage during baseflow conditions between the two dry WYs is higher than the difference between the two median WYs. The groundwater recharge starts two months earlier in the EoC driest WY compared to the historical driest WY due to the changes in timing and magnitude of precipitation. However, it is interesting to note that groundwater storage during baseflow conditions in the EoC WY is nearly equal to the historical WY (within 3%). Thus, although more water enters the EoC dry WY system through greater precipitation, it eventually exits by the end of the WY and no

606 considerable net gains to groundwater are observed. This significant reduction in groundwater  
607 storage from late winter to end-of-summer is a result of the much larger EoC *ET* and highlights  
608 the dynamic nature of the EoC dry year watershed interactions. Also similar to the median WY,  
609 dry WY seasonal decreases in EoC storage are more pronounced in the groundwater signal (36%)  
610 than in the surface water signal (33%). We further note that the decreases in groundwater and  
611 surface water storages are, as in the median WY, larger (+8%) than the historical decreases.

612

### 613 **3.3.3. Wet water years**

614 The EoC wet WY is significantly wetter than all other WYs. Yet, unlike the historical WY,  
615 the precipitation largely comes as rain, as shown by the low-to-no snowfall and *SWE* totals (Figure  
616 6). The difference in future versus contemporary wet WY *SWE* (99%) is larger than the differences  
617 between the median and the dry WYs (91%). As in other WYs, soil moisture increases earlier  
618 compared to the historical wet WY. A greater water availability enables the system to meet the  
619 high EoC *ET* demand. Hence, *ET* in the EoC wettest year remains higher than the historical wettest  
620 year *ET* throughout the WY. However, the increase in *ET*, combined with the lack of snowmelt  
621 that can buffer and recharge soil moisture in spring, leads to less soil moisture at the end of the  
622 WY compared with the historical WY. Further, surface water storage increases earlier and at a  
623 much faster rate in the EoC WY compared to the historical WY. This is mirrored in the  
624 groundwater storages. As in the other EoC simulations, when compared to the historical  
625 counterpart the EoC wettest year shows a sharper decline in seasonal above and below groundwater  
626 storage changes (occurring between peak flow and baseflow). Groundwater storage decreases 47%  
627 in the EoC between peak flow and baseflow, whereas only a 41% decrease occurs in the historical

628 wet WY. Similarly, surface water storage decreases 44% in the EoC whereas only a 41% decrease  
629 occurs in the historical wet WY.

630

### 631 **3.4. Spatial patterns of the changes in fluxes and pressure-heads**

#### 632 **3.4.1. Median water years**

633 To provide a deeper understanding of how the changes in precipitation timing, magnitude,  
634 and phase affect the land surface processes and surface and subsurface hydrodynamic responses,  
635 we assess the spatial patterns of these changes during two key periods in the WY, peak flow and  
636 baseflow. Figure 7 shows the percent changes in *ET*, surface water pressure-heads, and subsurface  
637 pressure-heads (i.e., pressure-heads of the model bottom layer) in the EoC median WY compared  
638 to the historical median WY during peak flow and baseflow conditions (see the time frames in  
639 Figure 6). Regions in red correspond to areas with smaller fluxes or pressure-heads in the EoC  
640 compared to the historical ones, whereas regions in blue correspond to areas with larger fluxes or  
641 pressure-heads in the EoC compared to the historical median WY. We study peak flow and  
642 baseflow conditions because the analysis of the temporal variations of fluxes and storages has  
643 shown that these two periods are characterized by different trends and represent the key periods in  
644 understanding the hydrologic responses to the EoC extreme climate.

645 Relative to the historical median WY, during peak flow the EoC median WY is  
646 characterized by an increased *ET* across the majority of the watershed, especially in the Central  
647 Valley, and larger surface water and subsurface pressure-heads (Figure 7a-c). *ET* increases in the  
648 EoC both because of the increase in water availability and increased evaporative demand, as  
649 discussed in the previous section (3.3.1.). The increase in *ET* is non-uniform across the watershed  
650 because of the heterogeneity of the landscape's topographical gradients, land-surface cover, and

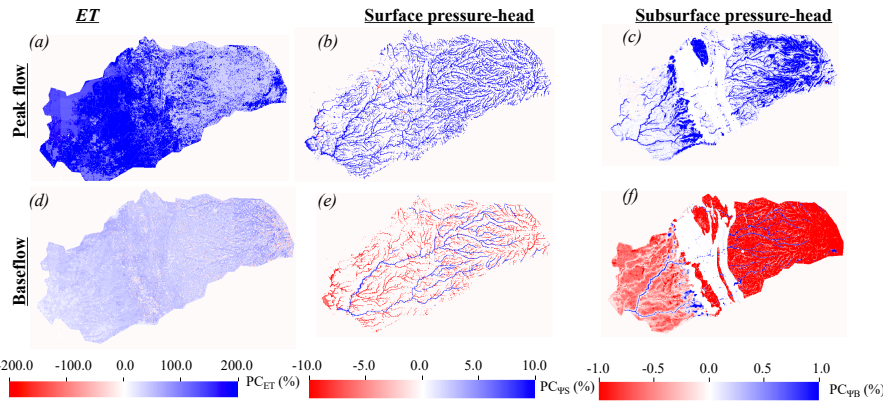


651 subsurface geological conditions. The Central Valley is characterized by a large increase in *ET*  
652 compared to the Sierra Nevada, and the patterns of *ET* in the Central Valley are also more  
653 homogeneous, a resultant of the geological characteristics of the area and the hydroclimate of the  
654 watershed (i.e., where most of the precipitation falls over the Sierra Nevada but follows  
655 topographic gradients downward into the valley where more recharge occurs). This leads to more  
656 water available in the Central Valley compared to the Sierra Nevada characterized by less  
657 permeable rocks. In addition, as most of the *ET* in the Central Valley comes from evaporation due  
658 to the high temperatures of the EoC (not shown here), the increase in evaporation is higher in the  
659 Central Valley due to its aquifers characterized by a high permeability (Maina and Siirila-  
660 Woodburn, 2020) and the availability of water.

661       Surface and subsurface pressure heads both show general increases during the EoC peak  
662 flow, yet these maps reveal that unlike *ET* the pressure head (and therefore storage) of water is  
663 very heterogeneous in space. For example, in the Sierra Nevada, we observe an increase in  
664 subsurface pressure-head (Figure 7c) only in some relatively permeable areas susceptible to  
665 infiltration and recharge. Although the Central Valley aquifers are more permeable and  
666 geologically less heterogeneous than the Sierra Nevada (as defined in the model), the changes in  
667 subsurface pressure-head in the Central Valley are heterogeneous. This is because the recharge of  
668 the Central Valley aquifers is dependent on the subsurface and surface flows from the headwater  
669 (i.e., connectivity to the headwater). In other words, only areas of the Central Valley that are  
670 subject to stronger connectivity with the headwaters see an increase in subsurface pressure-head  
671 in the EoC, likely because they are more regularly recharged by the headwaters through surface  
672 and subsurface flows from these areas, a recharge that buffers the water depletion through *ET*.

673 These are mostly the areas located close to the streams where there is an exchange between the  
674 subsurface and the surface and the Sierra Nevada foothills (in the alluvium 3 area, see Figure 1).

675 Relative to its historical counterpart, the EoC median WY is characterized by high *ET*  
676 during baseflow conditions though less than during peak flow conditions. (Figure 7d). We observe  
677 larger surface water pressure-heads in higher-order streams whereas surface water pressure-heads  
678 decrease in the EoC in the majority of the low-order, ephemeral streams (Figure 7e). This  
679 opposition of spatial pattern trends, resulting in more water in the main river channels, and less in  
680 the smaller streams, occurs for several reasons. First, peak flow occurs earlier in the EoC and is  
681 more rainfed, so that the ephemeral streams drain earlier in the EoC compared to in the historical  
682 period. This sustained and longer duration of draining increases the surface water pressure-head  
683 along the main river channels and is due to the contribution of the subsurface in the headwaters.  
684 This contribution is also higher in the EoC due to larger amounts of precipitation. The trends along  
685 the main river channel are also evident in the subsurface pressure-head maps (Figure 7f). Because  
686 the surface water is larger along the main channels, the subsurface pressure-heads are also larger  
687 here due to the interconnection between the subsurface and the surface (Figure 7f). However, in  
688 general, subsurface pressure-heads decrease elsewhere in the EoC during baseflow because of the  
689 lack of snowmelt and the higher *ET* demand. This result highlights the spatiotemporal complexity  
690 of an expected watershed's response to changes in climate (shown here to be bi-directional), and  
691 how factors such as river proximity may be crucial for consideration.



692

693 Figure 7: Comparisons between EoC median water year (WY) and the historical median WY peak  
 694 flow and baseflow spatial distributions of percent changes in  $ET$  ( $PC_{ET}$ ), surface water ( $PC_{\psi_S}$ ) and  
 695 subsurface ( $PC_{\psi_B}$ ) pressure-heads. Regions in red correspond to areas with smaller fluxes or  
 696 pressure-heads in the EoC compared to the historical ones, whereas regions in blue correspond to  
 697 areas with larger fluxes or pressure-heads in the EoC compared to the historical WY.

698

699

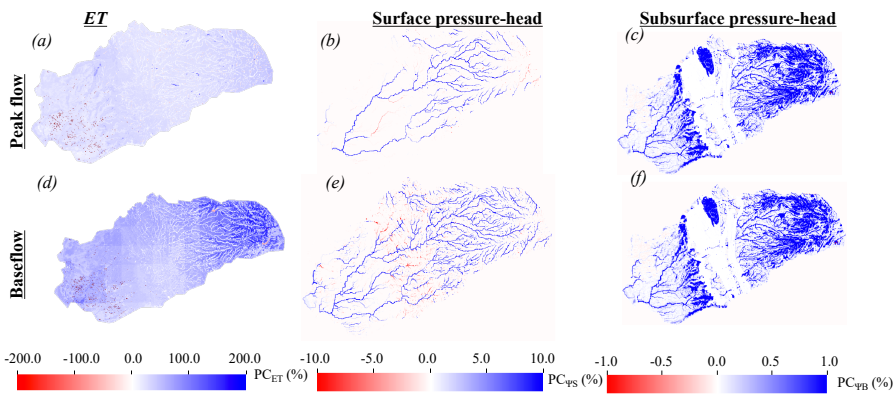
### 3.4.2. Dry water years

700

701 Figure 8 illustrates the percent changes in  $ET$ , surface water, and subsurface pressure-heads  
 702 in the EoC dry WY compared to the historical dry WY during peak flow and baseflow conditions.  
 703 During peak flow conditions, the EoC dry WY has larger  $ET$ , surface, and subsurface pressure-  
 704 heads than the historical dry WY (Figure 8a-c).  $ET$  is larger in this EoC dry WY not only because  
 705 it is hotter, but also because there is more precipitation, as noted previously. Increases in surface  
 706 pressure-heads are non-uniform across the domain. For example, surface water does not increase  
 707 in high elevation areas (i.e., elevation > 2000m) in the EoC dry WY because the change in the  
 precipitation phase is not significant. The main difference between the EoC and the historical dry

708 WY is the amount of the water flowing down gradient, which is higher in the EoC, hence the  
 709 surface water in the EoC becomes higher downstream. The increase in subsurface pressure-heads  
 710 in the EoC dry WY during peak flow conditions is heterogeneous with patterns similar to the  
 711 changes in subsurface pressure-heads associated with the EoC median WY.

712 During baseflow conditions, even though *ET* increases in the EoC driest WY relative to  
 713 the historical driest WY, surface, and subsurface pressure-heads also generally increase (Figure  
 714 8d-f). Given wetter conditions in the driest EoC WY, first-order streams are more pronounced. A  
 715 few low-order streams have less surface water in the EoC when compared to the historical dry  
 716 WY, similar to the results of the median WYs (see section 3.4.2). Subsurface pressure-head is  
 717 generally larger in areas subject to strong connectivity with the headwaters (i.e., receiving more  
 718 water from the headwaters through subsurface and surface flows) in the EoC dry WY relative to  
 719 the historical dry WY, with some regions experiencing no change from the historical conditions.  
 720 This suggests that the larger amount of precipitation associated with the EoC dry WY is sufficient  
 721 to supply enough water to account for high *ET* demands and recharge the groundwater.



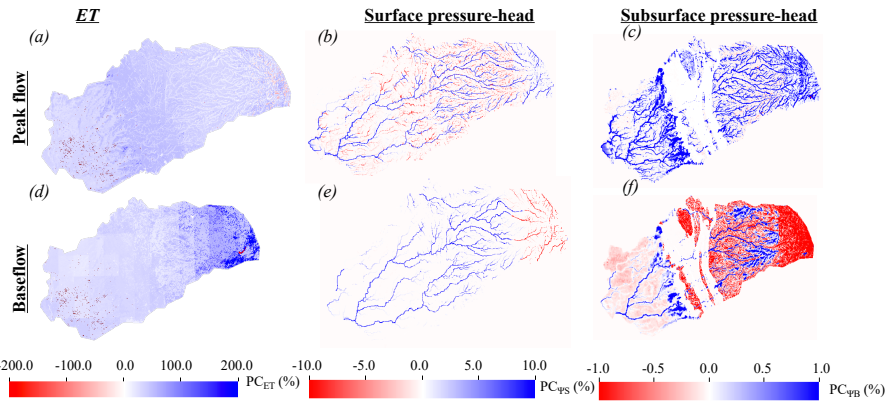
722  
 723 Figure 8: Comparisons between EoC dry water year (WY) and the historical dry WY peak flow  
 724 and baseflow spatial distributions of percent changes in *ET* ( $PC_{ET}$ ), surface water ( $PC_{\psi_s}$ ) and

725 subsurface ( $PC_{\psi B}$ ) pressure-heads. Regions in red correspond to areas with smaller fluxes or  
726 pressure-heads in the EoC compared to the historical ones, whereas regions in blue correspond to  
727 areas with larger fluxes or pressure-heads in the EoC compared to the historical WY.

728

### 729 **3.4.3. Wet water years**

730 Figure 9 shows the percent changes in  $ET$ , surface water, and subsurface pressure-heads in  
731 the EoC wet WY compared to the historical wet WY during peak flow and baseflow conditions.  
732 During peak flow, the EoC wet WY is characterized by larger  $ET$  and subsurface pressure-heads  
733 relative to the historical wet WY and a more heterogeneous mixture of regions with both higher  
734 and lower surface water conditions throughout the catchment (Figure 9 a-c). Analogous to other  
735 WYs at EoC, the surface water pressure-head increases (decreases) are apparent in larger-order  
736 (smaller order) streams, both in the Sierra Nevada and in the Central Valley. In the wettest WY,  
737 this occurs for several reasons. First, the larger volume of precipitation, plus seasonal shifts in  
738 precipitation timing result in the filling of the higher-order streams and depletion of the lower-  
739 order streams during peak flow. Second, in the historical wet WY, a significantly greater amount  
740 of snowpack is present in the Sierra Nevada in the upper elevation of the headwaters, allowing for  
741 slower, steadier amounts of water that is released during the spring via snowmelt, and in turn,  
742 supporting low-order streams over a longer period of time. The latter effect is immediately visible  
743 in Figure 9e, where decreases in EoC surface pressure heads are visible in the headwaters, despite  
744 the watershed-total showing an increase in EoC surface water storage during baseflow (see Figure  
745 6). Similar to the two previous EoC WYs, the subsurface pressure-head increases are shown more  
746 distinctly in the Central Valley during peak flow, under the main river channels, and in the foothills  
747 during baseflow (see previous sections on the discussion of hydroclimatic and geologic impacts).



748

749 Figure 9: Comparisons between EoC wet water year (WY) and the historical wet WY peak flow  
 750 and baseflow spatial distributions of percent changes in  $ET$  ( $PC_{ET}$ ), surface water ( $PC_{\psi_S}$ ) and  
 751 subsurface ( $PC_{\psi_B}$ ) pressure-heads. Regions in red correspond to areas with smaller fluxes or  
 752 pressure-heads in the EoC compared to the historical ones, whereas regions in blue correspond to  
 753 areas with larger fluxes or pressure-heads in the EoC compared to the historical WY.

754

755 **4. Discussion**

756 **4.1 Comparison with previous studies**

757 Some of the results presented in this study are qualitatively in agreement with previous  
 758 studies yet provide important new insights. For example, Maurer & Duffy, (2005) used 10 global  
 759 climate models to predict, as in this study, an increase in winter flows with an earlier peak flow  
 760 timing in the WY and a decrease in summer flows. Maurer & Duffy show that mid-century  
 761 projected annual precipitation and streamflow increases of 7% and 13% (respectively). Although  
 762 our study focused on EoC projections, we found that compared to the historical median WY,  
 763 annual surface water will increase by 19% in the EoC median WY. Compared to their findings,

764 our work sheds light on how these changes in runoff will occur across the watershed based on its  
765 physical characteristics and highlights that while runoff will increase in the EoC lower-order  
766 streams mainly located in the Sierra Nevada will see a decrease due to the change in the  
767 precipitation phase. Mallakpour et al., (2018) also had a similar finding in a study that shows that  
768 future California streamflow is altered similarly to Maurer & Duffy, (2005) under both the RCP4.5  
769 and RCP8.5 emissions scenarios, with RCP8.5 showing the highest changes during peak flow.  
770 However, contrary to our work the authors mentioned that the annual changes in streamflow will  
771 not be significant probably due to the compensation between increases in peak flow and decreases  
772 in baseflow. This was likely shaped by the differences in climate and hydrologic models used to  
773 derive these conclusions. Similar changes in streamflow were obtained by He et al., (2019) who  
774 drove the hydrologic model VIC with 10 global climate models to understand potential changes in  
775 runoff in California due to climate change. Hydrologic changes computed from the 10 global  
776 climate models were consistent and robust and showed an increase of around 10% in annual  
777 streamflow by the late century, a percentage similar to what has been found in this study. The  
778 authors mentioned that watershed characteristics such as geology, topography, and land cover  
779 strongly impact the hydrologic response to climate change. Relationships between watershed  
780 characteristics (e.g., physiographic parameters) and its responses to climate change were further  
781 explored by Son & Tague, (2019) who highlighted that because vegetation and subsurface geology  
782 control both water availability and energy demand, they in turn influence watershed sensitivity to  
783 a changing climate as shown in this study.

784         The increases in groundwater storage shown in this study are also in agreement with  
785 Niraula et al., (2017) who used the hydrologic model VIC to show that groundwater recharge will  
786 likely increase in the northern portion of the western United States in a changing climate. However,

787 contrary to their work that estimates changes in groundwater recharge over a large domain (i.e.,  
788 the western United States). In this work, we show that groundwater recharge decreases in the  
789 summer in some areas due to the lack of snowmelt and high EoC *ET*. Increases in *ET* in response  
790 to global warming were also documented by Pascolini-Campbell et al., (2021) who showed a 10%  
791 increase in global *ET* from 2003 to 2019.

792 An advantage of our approach is a more explicit estimate of spatiotemporal changes in  
793 groundwater-surface water feedbacks because Parflow-CLM physically solves the transfer and  
794 movement of water from the bedrock to the canopy. Additionally, the aforementioned studies used  
795 different emission scenarios and models to project changes in hydrology, nonetheless, their results  
796 have shown that the directions of the observed changes are consistent across models and emission  
797 scenarios and only the magnitude of these changes is uncertain. Hence, the trends observed in this  
798 study using a single model and emission scenario likely represent the trends we would observe  
799 using different models and scenarios. While our results show similar patterns and changes, our  
800 study provides a much finer-grained perspective on the sensitivity of a watershed to changes in  
801 climate extremes based on its subsurface geology, topography, and land cover. It also highlights  
802 that the spatiotemporal analyses of these changes may reveal different trends than if only assessed  
803 as annual changes. Understanding these localized changes and sensitivities is critical and has  
804 practical implications for water management.

805

#### 806 **4.2 Implications for water resources management**

807 Because our work provides a better understanding of the spatiotemporal changes in  
808 hydrodynamics in response to future extremes, our findings also have important implications for  
809 water resources in California. While previous work more broadly focused on how temperature



810 increases will alter the precipitation phase and reduce seasonal snowpack and increase winter  
811 runoff, this work brings new physical and more granular insights into how watersheds may respond  
812 to climate extremes. In particular, both wet and dry WYs in the future experience increased  
813 precipitation. As such, even in future dry WYs, water managers and stakeholders may need to  
814 prepare more for large precipitation events that may increase the possibility of flooding and require  
815 new infrastructure management strategies. For example, in a future where WYs are generally  
816 wetter, having alternatives for water supply during periods of sustained drought could be less  
817 important. However, as we show in this paper, shifts in precipitation timing, phase, and magnitude  
818 have cascading impacts on soil moisture profiles and *ET* withdrawals, which subsequently impact  
819 discharge and groundwater dynamics. Future shifts in water availability earlier in the year, as well  
820 as more dynamic transitions between peak and baseflow conditions (as quantified here), may  
821 impose stresses on water distribution, especially those systems already under scrutiny (e.g. those  
822 resources over-allocated or facing environmental degradation).

823         In addition, while these projections show increases in surface water and groundwater  
824 storages at watershed-scale, our results also highlight important localized spatiotemporal changes  
825 across a watershed, where the assumption of water storage increase does not necessarily hold in  
826 all geographic locations (e.g., areas that are not close to the river in the Central Valley). Our study  
827 also shows that the decreases in groundwater storage in the Central Valley aquifers are more  
828 significant than the decreases in surface water storage during baseflow conditions. This may call  
829 for new conveyance infrastructure that can move water from the relatively wetter areas to the drier  
830 areas and/or where infiltration can more readily occur. The latter suggests solutions such as  
831 Managed Aquifer Recharge (MAR) could become an increasingly important climate change  
832 adaptation. Finally, our study also highlights that lower-order streams will likely become more

833 ephemeral in the EoC due to flashier runoff and higher evaporative demand, such conditions will  
834 have important implications for fish spawning and ecosystem nutrient cycling. Although our  
835 results are embedded with uncertainties and are based on a single projection and model, they do  
836 highlight the need for a revisit of current water management strategies. Further studies using  
837 different climate and land-use scenarios and models of varying complexity and resolution could  
838 help build more confidence and provide more information in defining how future water  
839 management strategies would need to change to be more resilient to more extreme WYs in the  
840 future.

841

#### 842 **4.3 Study limitations**

843 This study combines novel climate and hydrologic simulations that provide both  
844 advantages and disadvantages compared with previous work (He et al., 2019; Maurer & Duffy,  
845 2005; Niraula et al., 2017; M. Safeeq et al., 2014; Son & Tague, 2019). We note several of these  
846 disadvantages below. In the integrated hydrologic model, the subsurface geology and land cover  
847 characterization has inherent and, in some cases, irreducible uncertainty. This study uses  
848 hydrodynamic parameters as defined by Maina et al. (2020a), which assumes that the subsurface  
849 hydrodynamics from the Sierra Nevada to the Central Valley is almost completely hydrologically  
850 separated except through overland flow. However, it is not clear whether fractures or other  
851 macrostructures may drive more surface and subsurface flows from the headwaters to the Central  
852 Valley aquifers. In addition, we use the historical land surface cover map when simulating the  
853 EoC. Since vegetation will dynamically respond to a changing climate, the land surface cover used  
854 in the EoC simulations may be unrealistic and may influence, for example, *ET* and/or soil moisture.  
855 For example, it has been shown that the stomatal resistance of plants will change due to rising CO<sub>2</sub>

856 with important implications for both the water and energy balance (Lemordant et al., 2018; Milly  
857 & Dunne, 2017). Yet, our use of historical land surface cover does have the advantage of isolating  
858 changes in fluxes associated with climate change alone and could be compared in future work with  
859 additional simulations that account for both changes in the land surface and climate. Future studies  
860 will assess the impact of changes in vegetation physiology and land surface cover on watershed  
861 hydrodynamics. In this study, we did not include the impacts of anthropogenic activities such as  
862 pumping and irrigation due to the uncertainties in predicting these fluxes in EoC. While these  
863 human interventions could substantially change the hydrologic system, our study isolates the  
864 impacts of a changing climate on the natural system. Future studies can now estimate the impacts  
865 of different pumping and irrigation scenarios at EoC that may further impact the hydrologic system  
866 hydrodynamics in a changing climate and compare and contrast with this work. Although our VR-  
867 CESM simulations represent a cutting-edge global climate model simulation (e.g., 28 km regional  
868 grid-refinement, coupled atmosphere-land simulation with prescribed ocean conditions, etc.),  
869 further work may be needed to evaluate how a more refined grid resolution impacts atmospheric  
870 process representation over the Cosumnes watershed, particularly in the headwaters (Maina et al.,  
871 2020b). We further acknowledge that the 30-year simulation may not be sufficient to capture  
872 certain climate extremes (e.g., 1-in-50-year storm). Future studies, if computational resources are  
873 available, will seek to explore how the use of a longer time period might influence the  
874 identification of the most extreme dry and wet WYs from VR-CESM.

875 In this study, we relied on deterministic models to represent both the atmospheric (VR-  
876 CESM) and hydrologic (ParFlow-CLM) dynamics. These models are very sensitive to the initial  
877 conditions and input parameters (La Follette et al., 2021; Lehner et al., 2020; Song et al., 2015)  
878 which are uncertain given the lack of data characterizing the above and below-ground

Deleted: Last, a

Formatted: Font color: Text 1

Formatted: Indent: First line: 0.5"

Formatted: Font color: Text 1

Formatted: Font color: Text 1

880 environment, including its hydrological response. Thus, while it is important to assess the  
881 sensitivity of the model outputs to these uncertain parameters, these models are computationally  
882 expensive and require many parameters. For example, a complete sensitivity analysis of the  
883 hydrologic model requires running it thousands of times to explore the full parameter space (which  
884 has a dimension of over 29). Such an approach is not feasible with the currently available  
885 computational resources because it takes longer than one wall-clock day to simulate a single water  
886 year for a single model parameterization, even in a high-performance computing environment.  
887 Future work could employ reduced order models based on a subset of the physics-based model  
888 runs to explore parameter space further (e.g. Maina et al., 2022). In addition, because of the  
889 behavior of hydrological processes, the climate variability, and the uncertainties of deterministic  
890 models, model validation should ideally be performed over a long period to account for different  
891 changes and variabilities. In this study, model validation was limited to a period of 5 years due to  
892 computational constraints. Although this period encompasses the wettest and driest years on record  
893 in the region, we acknowledge that it may not be sufficient to capture the full range of hydrological  
894 variability. Another limitation of using deterministic models is that the temporal variations of  
895 hydrological processes tend to follow a stochastic behavior in accordance with the so-called Hurst  
896 phenomenon (Hurst, 1951; Koutsoyiannis, 2003). As a result, the use of deterministic models such  
897 as the ones employed in this study could intensify the impacts of hydrological extremes and climate  
898 change. Finally, it has also been demonstrated that while the changes in water balance exhibit  
899 greater variability on climatic scales, the most important changes in hydrologic processes remain  
900 the overexploitation of groundwater (Ferguson and Maxwell, 2010) which has an impact on the  
901 rise in sea level (Koutsoyiannis, 2020). In addition to projecting the use of groundwater by the end

Formatted: Font color: Text 1

Formatted: Font color: Text 1

902 of the century, future studies could compare the two approaches (deterministic and stochastic) to  
903 better assess the limitations and the uncertainties associated with them.

Deleted: ¶

## 904 **5 Summary and Conclusions**

905 The effects of climate change are increasingly felt across many regions of the world,  
906 especially in hydrologically sensitive regions with Mediterranean climates such as California.  
907 Many studies over the years have been conducted to better understand the hydroclimate of the EoC  
908 and its impacts on the hydrologic cycle. Previous studies have used a multitude of different models  
909 at varying complexity and climate scenarios to highlight that the future climate has multiple  
910 plausible outcomes. Most of these studies indicate warmer temperatures and precipitation that  
911 mostly falls as rain instead of snow. For example, the state of California is projected to experience  
912 more punctuated climate extremes coupled with a marked decrease in the Sierra Nevada snowpack  
913 (Cayan et al., 2008; Gleick, 1987; Musselman, Molotch, et al., 2017; Rhoades, Ullrich, &  
914 Zarzycki, 2018). Such drastic transitions have already started to shape the hydroclimate of  
915 California. Faced with this new normal, it is becoming increasingly important to assess how the  
916 integrated hydrologic cycle may respond to these perturbations and connect these responses more  
917 directly to water resource management, particularly with modeling frameworks that can better  
918 represent the interactions between the changing atmosphere and the surface and subsurface  
919 hydrology.

920 In this work, we used state-of-the-art physics-based models at high resolutions for their  
921 respective communities to project changes in meteorological conditions at the EoC and assess how  
922 their combined effects influence watershed hydrology from the land surface to the deeper  
923 subsurface. Importantly, our approach to couple a variable resolution Earth System Model and an  
924 integrated hydrologic model allow for us to simulate hydro-meteorological conditions which are

926 jointly driven by thermodynamical and dynamical shifts in climate. We model the Cosumnes  
927 watershed, which spans the Sierra Nevada and Central Valley and hosts one of the last rivers in  
928 the state without a large dam, as a testbed to understand how climate drivers will impact water  
929 resources in the EoC. We performed climate simulations over 30-year periods historically (1985-  
930 2015) and at EoC (2070-2100) and identified the driest, median, and wettest WYs from those  
931 simulations, which were then used as meteorological forcing for the hydrologic model. Our  
932 coupled simulations project that, for the Cosumnes watershed, temperature and precipitation will  
933 both increase by the EoC across all WY types (wettest, median, and driest). In addition,  
934 precipitation is projected to fall earlier compared to historical conditions and mainly in the form  
935 of rain. For the median and wet WYs the precipitation season has earlier cessation dates, while the  
936 dry EoC WY, which is wetter than its historical counterpart, persists significantly longer into the  
937 spring. As a consequence of warmer temperatures, all WYs show a substantial decrease in *SWE*.  
938 The shift of precipitation from snowfall to rainfall, as well as the increase in the amount of  
939 precipitation and the early start of precipitation lead to an overall increase in soil moisture and  
940 more water available to meet the higher EoC *ET* demand. Importantly, this increase in *ET* is  
941 heterogeneous across the watershed and highlights one of the main advantages of using an  
942 integrated hydrologic model such as the one we employed in this study to assess the spatiotemporal  
943 patterns of change. Our results show that the sensitivity to the changes in *ET* at EoC depends on  
944 the subsurface geology and topographical gradients. More specifically:

- 945 • The geological and topographical complexities of the Sierra Nevada headwaters  
946 lead to highly heterogeneous changes in *ET*. Changes in *ET* are higher in permeable  
947 areas such as the plutonic rocks where water can be more easily extracted.

948           • *ET* changes in the Central Valley of the Cosumnes watershed are predominantly  
949           uniform with the highest sensitivities in the vicinity of the Cosumnes River due to  
950           the high availability of water.

951           Precipitation increases enough in the EoC to provide water for both increased *ET* and  
952           increased surface water storage. Surface water storages also increase earlier in the WY and have  
953           higher peak amounts. This earlier and larger increase is a direct consequence of an earlier start in  
954           precipitation at EoC, a marked change in the precipitation phase, and an overall larger amount of  
955           precipitation when compared with the historical WYs. However, our results also highlight that  
956           during baseflow conditions surface water decreases, especially in lower-order streams, showing  
957           that these areas are highly sensitive to the change in precipitation phase. Our simulations also show  
958           that the seasonal variability of the EoC watershed behavior is also more dynamic. In general,  
959           decreases in seasonal water storages occurring between peak flow and baseflow conditions are  
960           more than 10% higher in the EoC compared to the historical conditions.

961           EoC groundwater storages are also projected to increase earlier in the WY with peaks  
962           greater than those found historically. Yet these storages decrease significantly during baseflow  
963           conditions due to the higher *ET* at EoC and the absence of recharge from snowmelt. Contrary to  
964           the changes in surface water storages, groundwater storages show a larger decrease due to their  
965           dependence on the surface water from the Sierra Nevada. Our results also show that changes in  
966           subsurface pressure-heads are not uniform and are bi-directional throughout the Cosumnes  
967           watershed. Because the connectivity between the Central Valley aquifers and the Sierra Nevada  
968           headwaters (i.e., subsurface and surface flows from the headwater to the Central Valley aquifers)  
969           plays an important role in the hydrodynamics of this watershed, only areas with a strong connection  
970           with the headwaters, such as the foothills and the river channels, see an increase in subsurface

971 pressure-heads at EoC. However, the subsurface pressure-heads decrease elsewhere in the Central  
972 Valley aquifers especially in baseflow conditions due to the high *ET* and the lack of snowmelt. In  
973 the river channels, this is due to the exchange between the subsurface and the surface whereas the  
974 foothills characterized by the consolidated sediments serve as “spillover.”

975 Our results provide novel understandings about possible changes in the integrated  
976 hydrologic response to changes in EoC climate extremes. An important caveat is that our  
977 simulation was a single set of climate realizations and may not properly bound internal variability  
978 uncertainty like an ensemble of climate simulations could. However, beyond the widely agreed-  
979 upon changes of decreased snowpack and shifts in runoff timing in the literature, we show that in  
980 this simulation: 1) EoC precipitation increases even in the driest years; 2) despite an increased  
981 temperature, and hence *ET*, both groundwater and surface water storage increase relative to  
982 historical conditions because of increased precipitation; and 3) there is a distinct spatial pattern,  
983 particularly in surface water storage, in which smaller-order streams see reduced flow while the  
984 larger order streams see an increased flow. These changes will have strong implications on natural  
985 resource management.

986 In this study, land cover changes are assumed to not occur, however, changes in land cover  
987 are expected to occur in the future, either naturally or anthropogenically. Further vegetation  
988 physiology will also change in response to an increase in CO<sub>2</sub>. Thus, future studies should  
989 investigate the impacts of these changes and how they may further alter the integrated hydrologic  
990 budgets. Additionally, future studies could also assess the effects of anthropogenic activities such  
991 as pumping and irrigation under a changing climate, other emissions scenarios, and/or the  
992 sequencing of variable end-member WYs and the interannual memory of the hydrologic system.  
993 Importantly, an understanding of this variability could be used to inform how water managers

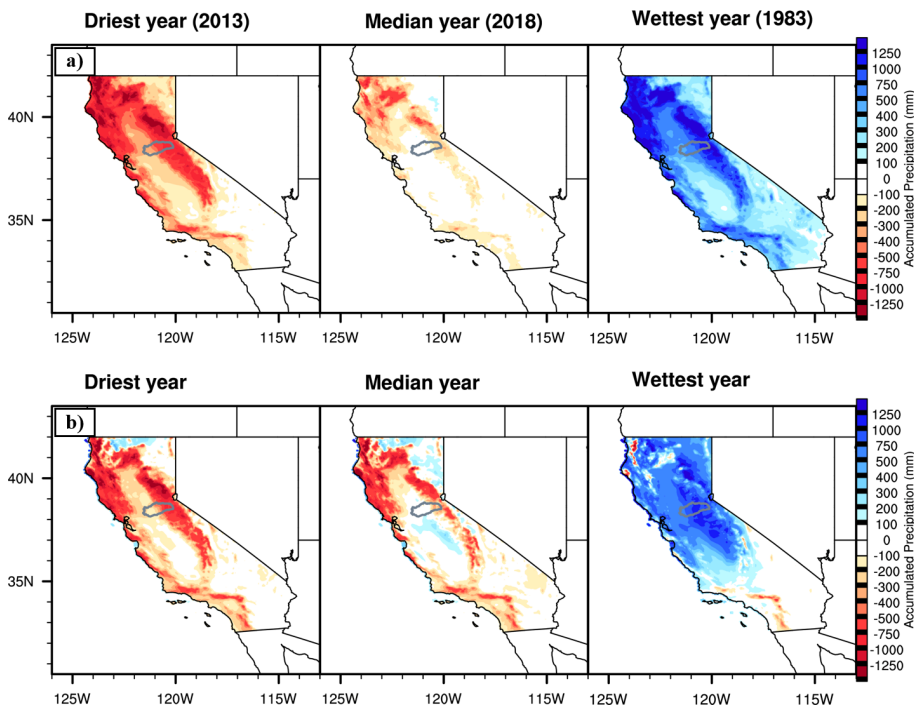


994 might prepare for more intense and/or intermittent extremes in the future. Future research could  
995 also use multiple emission scenarios to better assess the range in hydrodynamic responses  
996 dependent on the severity of climate change, especially those related to the magnitude and spatial  
997 location of the precipitation response since they are likely more uncertain and scenario-dependent  
998 than the trends at the watershed-scale.

999           **Appendix A: Comparisons between VR-CESM and PRISM historical conditions**

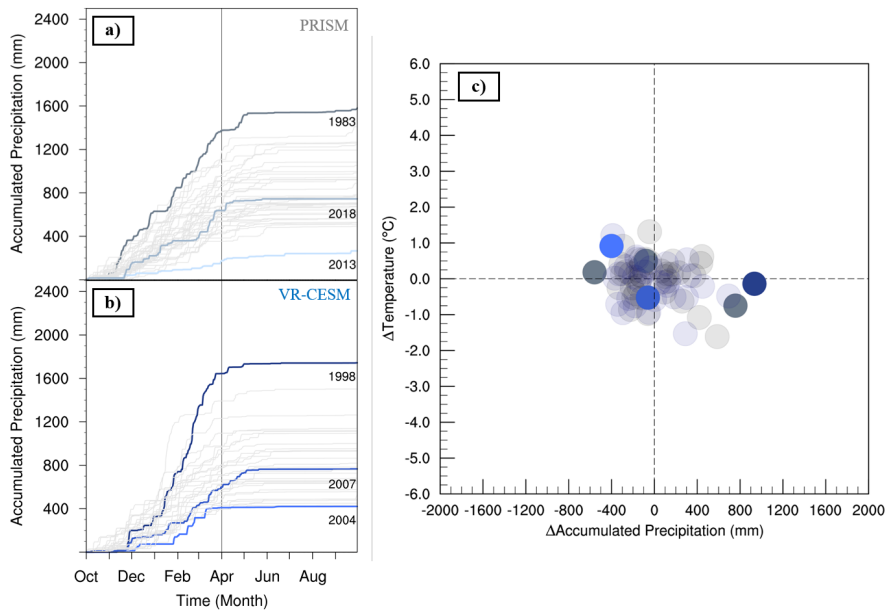
1000           Figure A1 highlights differences in dry, median, and wet WY accumulated precipitation  
1001 relative to the 1981-2019 PRISM climatology. VR-CESM generally recreates the spatial pattern  
1002 of anomalous dry and wet patterns across California for each WY type. This is shown via the  
1003 common regions of minimum and maximum anomalies relative to the PRISM climatology.  
1004 Notably, there are regions where VR-CESM anomalies are not consistent with PRISM. This is  
1005 primarily shown in the wettest water year in portions of the Central Valley, western slopes of the  
1006 Sierra Nevada, and southern California. This is likely correlated with resolution and the lack of  
1007 orographic gradients (both valleys and peaks) in VR-CESM at 28km resolution. Mismatches in  
1008 accumulated precipitation may also be due to representation of atmospheric rivers (ARs) in VR-  
1009 CESM that were found to be generally larger, slightly more long-lived and make landfall more  
1010 frequently over California (Rhoades et al., 2020b). Figure A2 shows Cosumnes watershed WY  
1011 accumulated precipitation and surface temperature. WY accumulated precipitation is shown in  
1012 Figure A 2a and 2b for PRISM and VR-CESM, respectively. All WY accumulated precipitation  
1013 simulated by VR-CESM over 1985-2015 are within the range in PRISM, save for the wettest WY.  
1014 This is shown more explicitly in quadrant space in Figure A2c where the range of annual bias in  
1015 VR-CESM relative to the range of interannual variability in PRISM for accumulated precipitation  
1016 and temperature is shown. VR-CESM generally simulates a wetter historical period over the  
1017 Cosumnes (range of bias of 1330 mm) relative to PRISM (range of interannual variability of 1320  
1018 mm). Basin-average minimum (421 mm) and maximum (1740 mm) WY accumulated  
1019 precipitation are slightly larger than is found in PRISM. Of relevance to this study, PRISM has  
1020 shown notable uncertainties in the Sierra Nevada. Lundquist et al., 2015 showed that an  
1021 underrepresentation of the most extreme storm total precipitation in the Sierra Nevada can result

1022 in an upper-bound uncertainty of 20% in WY accumulated precipitation. Therefore, the wettest  
1023 WY of VR-CESM is well within the 20% uncertainty range of PRISM's wettest WY ( $1580 \pm 316$   
1024 mm). Further, differences in basin-average WY accumulated precipitation between VR-CESM  
1025 and PRISM are non-significant using a t-test and assuming a p-value  $< 0.05$ . The range of  
1026 temperature bias in VR-CESM ( $2.74\text{ }^{\circ}\text{C}$ ) relative to the range of PRISM interannual variability  
1027 ( $2.93\text{ }^{\circ}\text{C}$ ) was also within the temperature uncertainties discussed in Strachan and Daly, 2017.  
1028 They showed that a general cool-bias in PRISM temperatures were found on the leeward side of the  
1029 Sierra Nevada when compared with 16 out-of-sample in-situ observations across an elevation  
1030 gradient of 1950 to 3100 meters with an overall mean bias of  $-1.95\text{ }^{\circ}\text{C}$  (maximum temperature)  
1031 and  $-0.75\text{ }^{\circ}\text{C}$  (minimum temperature).



1032

1033 Figure A1: Differences in the driest, median, and wettest water year accumulated precipitation  
 1034 over California in a) PRISM and b) VR-CESM relative to the 1981-2019 PRISM climatology.  
 1035 The Cosumnes watershed boundary is outlined in gray.



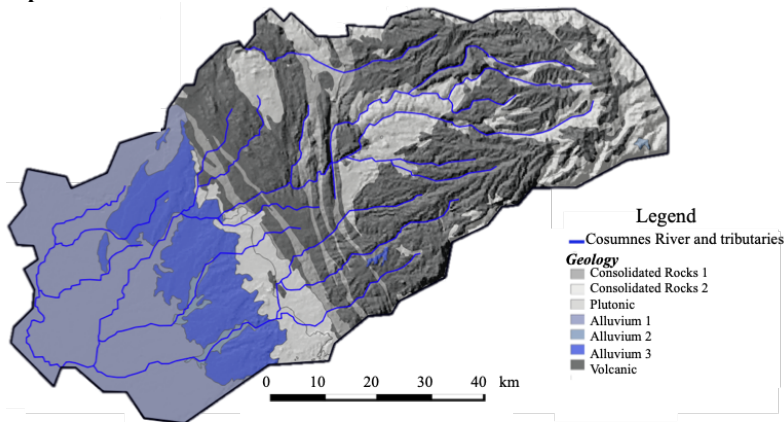
1036  
 1037 Figure A2: Cosumnes watershed accumulated precipitation totals in a) PRISM (gray; 1981-2019)  
 1038 and b) VR-CESM (blue; 1985-2015) with dry, median, and wet years emboldened. c) shows  
 1039 differences in PRISM (gray) and VR-CESM (blue) relative to the PRISM climatology (1981-2019)  
 1040 in temperature and accumulated precipitation quadrant space. Dry, median, and wet water years  
 1041 are emboldened.

1042

1043

1044 **Appendix B: Integrated Hydrologic Model Parameterization**

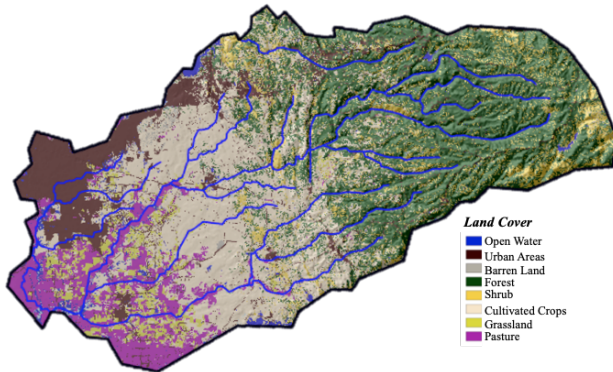
1045 **1. Input Variables**



1046 Figure B1: Geological map of the Cosumnes watershed (source: USGS, Jennings et al., 1977)  
 1047  
 1048

<b>Hydrodynamic properties based on the geology</b>				
Geological Formation	Porosity (-)	Specific Storage ( $m^{-1}$ )	Van Genuchten $\alpha$ ( $m^{-1}$ )	Van Genuchten $n$ (-)
Bedrock (Consolidated, Plutonic and Volcanic Rocks)	0.02	$10^{-6}$	3.0	3.0
Alluvial aquifers	0.2	$10^{-4}$	3.0	3.0

1049 Table B1: Assigned values of hydrodynamic parameters (porosity, specific storage and Van  
 1050 Genuchten parameters). Values are based on literature review (Faunt et al., 2010; Faunt and  
 1051 Geological Survey (U.S.), 2009; Flint et al., 2013; Gilbert and Maxwell, 2017; Welch and Allen,  
 1052 2014).



1053 Figure B2: Cosumnes watershed characteristics: land use and land cover (source: Homer et al.,  
 1054 2015), and model boundaries.  
 1055  
 1056

Surface roughness based on land use				
Land Use		Manning Coefficient ( $\text{h.m}^{-1/3}$ )		
Forest		$5 \times 10^{-2}$		
Shrub land and agricultural area		$5 \times 10^{-3}$		
Urban areas		$5 \times 10^{-5}$		
Crop properties				
Crop Type and Reference		Height (m)	Maximum Leaf Area Index (-)	Minimum Leaf Area Index (-)
Alfalfa (Evelt et al., 2000; Orloff, 1995; Robison et al., 1969)		0.6	6.0	2.0
Pasture (Buermann et al., 2002; King et al., 1986; Rahman and Lamb, 2017)		0.12	6.0	1.0
Vineyards (Johnson and Pierce, 2004; Vanino et al., 2015)		0.9	3.0	0.6

1057 Table B2: Manning coefficients and crop properties  
 1058

Boundary conditions	Value
Mokelumne and American river	Weekly-varying Dirichlet boundary conditions. These values are based on the measured river stages.
Sierra Nevada limit	No flow Neumann boundary condition
Bottom of the model	No flow Neumann boundary condition

1059 Table B3: boundary conditions  
 1060  
 1061  
 1062

## 2. Numerical model set-up

1063

Domain size	~7000 km <sup>2</sup>								
Spatial discretization	200 m horizontal from 0.1 m to 30 m in the vertical direction								
	Vertical Resolution								
	Layer	1	2	3	4	5	6	7	8
$\Delta z(m)$	0.1	0.3	0.6	1.0	8.0	15.0	25.0	30.0	
Simulation time	Model validation (from water year 2012 to water year 2017), then future water years								
Temporal discretization	hourly								

1064  
1065  
1066  
1067

Table B4: Numerical model discretization

**3. Output variables**

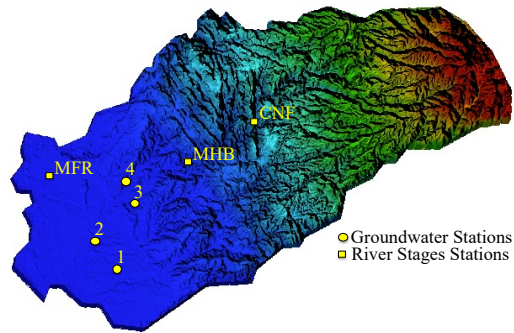
Selected output variables	Temporal scale	Spatial scale
Snow Water Equivalent	Yearly, monthly, and hourly	Domain-average and point scale
Evapotranspiration	Yearly, monthly, and hourly	Domain-average and point scale
Soil Moisture	Yearly, monthly, and hourly	Domain-average and point scale
River Stages (also surface water storages)	Yearly, monthly, and hourly	Domain-average and point scale
Groundwater levels variations (also subsurface storages)	Yearly, monthly, and hourly	Domain-average and point scale

1068  
1069  
1070  
1071

Table B5: Selected output variables

1072 **Appendix C: Integrated Hydrologic Model Validation**

1073 We compared temporal variations of streamflow at 3 stations located in the Sierra  
1074 (uplands), the intersection between the Sierra and the Central Valley, and the outskirts of  
1075 Sacramento (see Figure C1). Four wells in the watershed (see Figure C1) have reasonable, publicly  
1076 available records of groundwater levels and were used to check the ability of the model to  
1077 reproduce water table depth variations.



1078  
1079 Figure C1: The locations of the 3 streamflow gauges (CNF, MHB, and MFR) and 4  
1080 groundwater wells (stars).

1081  
1082 Figure C2a depicts the comparisons between simulated and measured river stages at the 3  
1083 stations indicated in figure C1. Absolute errors (L1) in m and relative errors (L2) are shown in  
1084 Table C1. Differences between simulated and measured streamflow vary between 0.4 and 0.8 m  
1085 (Table C1) indicating that the model is able to reproduce the river dynamics.

1086 Absolute differences given by:

1087 
$$L_{1i,j} = |X_{mes_{i,j}} - X_{sim_{i,j}}| \quad (C1)$$

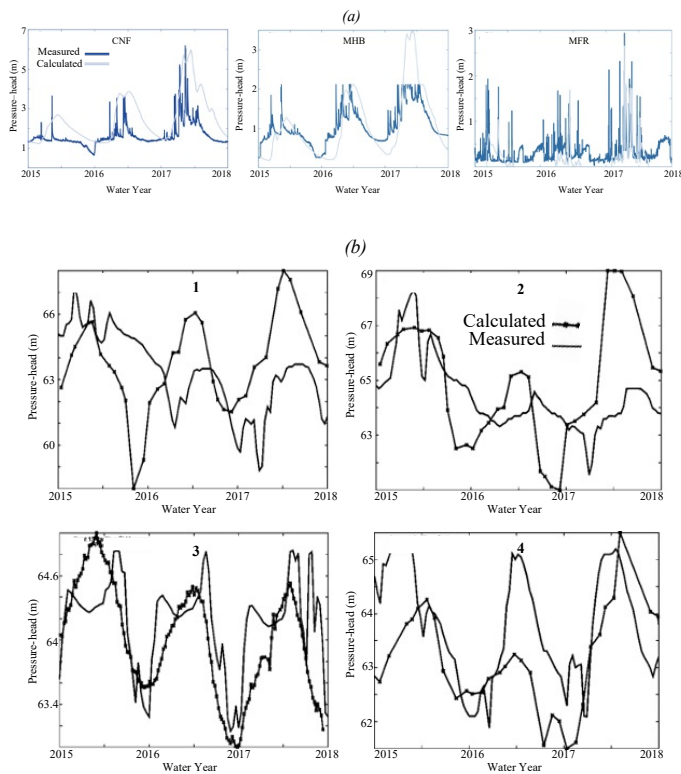


1088 Where  $L_{1,i,j}$  is the absolute difference associated with cell  $i$  and time  $j$ ,  $X_{mes_{i,j}}$  is the  
 1089 measured (or remotely sensed) data, and  $X_{sim_{i,j}}$  the simulated value.

1090 Relative differences  $L_{2,i,j}$  are given by:

1091 
$$L_{2,i,j} = \frac{|X_{mes_{i,j}} - X_{sim_{i,j}}|}{X_{mes_{i,j}}} \quad (C2)$$

1092



1093

1094 Figure C2: Comparisons between measured and calculated (a) river stages (i.e., pressure-  
 1095 heads simulated by ParFlow-CLM) and (b) subsurface pressure-head. The location of the selected  
 1096 points is indicated in Figure C1.

1097

<b>Measurements</b>	<b>L<sub>1</sub> (m)</b>	<b>L<sub>2</sub> (-)</b>
River Stages (CNF)	0.8	0.5
River Stages (MHB)	0.4	0.36
River Stages (MFR)	0.57	1.06
Groundwater Levels (Well 1)	3.73	0.05
Groundwater Levels (Well 2)	1.63	0.02
Groundwater Levels (Well 3)	0.476	0.0077
Groundwater Levels (Well 4)	1.08	0.016

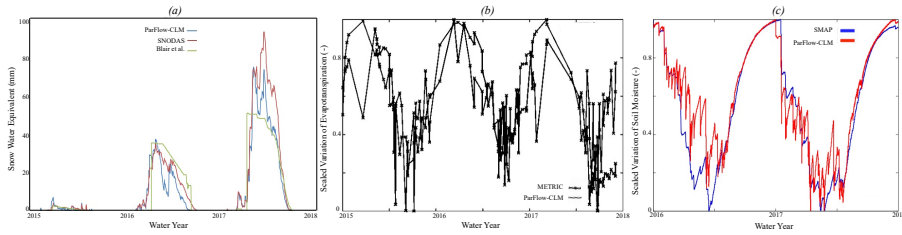
1098 Table C1: Differences between measured and calculated surface and groundwater levels. L1 is the  
1099 absolute error and R2 the relative error.

1100

1101 Comparisons between simulated and calculated groundwater levels (here referred to as the  
1102 pressure-heads at the bottom of the domain) shown in Figure C2b indicate that the model has  
1103 reasonable agreements with measurements. As shown in table C1, the error varies between 0.47 to  
1104 3.73 m depending on the station. Mismatches between simulated and observed groundwater levels  
1105 at wells 1 and 2 are likely due to an inaccurate estimation of pumping in these areas. The temporal  
1106 variations of the groundwater levels show an impact of withdrawals but because these withdrawals  
1107 are hard to estimate the model isn't correctly reproducing these trends.

1108 ParFlow-CLM also solves the key land surface processes governing the transfer of water  
1109 and energy at the land-atmosphere-soil interface: evapotranspiration, snow dynamics, and soil  
1110 moisture. In Maina et al., (2020a), rigorous comparisons between the ParFlow-CLM simulated  
1111 land surface processes and remotely sensed estimates of these variables were conducted (Figure

1112 C3). Table C2 shows the correlation coefficient between ParFlow-CLM results and the various  
 1113 datasets compared.



1114  
 1115 Figure C3: (a) Comparisons between domain-averaged total snow water equivalent obtained with  
 1116 ParFlow-CLM, SNODAS and Bair et al., reconstruction, (b) Comparisons between actual  
 1117 evapotranspiration obtained with ParFlow-CLM and METRIC (c) Relative variation of soil  
 1118 moisture obtained with ParFlow-CLM and SMAP. Note that the x-axis of (c) is shorter because of  
 1119 the availability of SMAP data

Satellites based products	L <sub>1</sub> (m)	L <sub>2</sub> (-)	Pearson Correlation Coefficient
SWE SNODAS (mm)	3.09	3.77	0.97
SWE Bair et al., (mm)	3.80	2.69	0.84
Soil Moisture SMAP (-)	0.217	3.07	0.94
ET METRIC (mm/s)	0.067	1.40	0.6

1120 Table C2: differences between measured and remotely sensed evapotranspiration (METRIC), soil  
 1121 moisture (SMAP), and snow water equivalent (SNODAS and Bair et al., 2016)

1122

1123 **Data availability**

1124 Data supporting the findings of this study can be found here:

1125 <https://portal.nersc.gov/archive/home/a/arhoades/Shared/www/Hyperion/>

1126           **Author contribution**

1127           The authors contribute equally to this work.

1128           **Competing interests**

1129           The authors declare that they have no conflict of interest.

1130           **Acknowledgements**

1131   Fadji Zaouna Maina and Erica Siirila-Woodburn were supported by LDRD funding from Berkeley  
1132   Lab, provided by the Director, Office of Science, of the U.S. Department of Energy under Contract  
1133   No. DE-AC02-05CH11231.

1134   Author Alan M. Rhoades was funded by the Department of Energy, Office of Science Office of  
1135   Biological and Environmental Research program under Award Number DE-SC0016605 "A  
1136   framework for improving analysis and modeling of Earth system and intersectoral dynamics at  
1137   regional scales" and Award Number DE-AC02-05CH11231 "The Calibrated and Systematic  
1138   Characterization, Attribution, and Detection of Extremes - Science Focus Area".

1139   This research used computing resources from the National Energy Research Scientific  
1140   Computing Center, a DOE Office of Science User Facility supported by the [http://](http://dx.doi.org/10.13039/100006132)  
1141   [dx.doi.org/10.13039/100006132](http://dx.doi.org/10.13039/100006132) of the U.S. Department of Energy under Contract No. DE-  
1142   AC02-05CH11231.

1143  
1144  
1145

1146           **References**

- 1147   Abbott, M. B., J. C. Bathurst, J. A. Cunge, P. E. Oconnell, and J. Rasmussen (1986), An  
1148           introduction to the european hydrological system: Sys- teme hydrologique Europeen, She  
1149           .2. Structure of a physically-based, distributed modeling system, *J. Hydrol.*, 87(1–2), 61–  
1150           77.
- 1151   Allan, R.P., Barlow, M., Byrne, M.P., Cherchi, A., Douville, H., Fowler, H.J., Gan, T.Y.,  
1152           Pendergrass, A.G., Rosenfeld, D., Swann, A.L.S., Wilcox, L.J. and Zolina, O. (2020),  
1153           Advances in understanding large-scale responses of the water cycle to climate change.  
1154           *Ann. N.Y. Acad. Sci.*, 1472: 49-75. <https://doi.org/10.1111/nyas.14337>
- 1155   Allen R. G., Masahiro T., Ricardo T. (2007)Satellite-based energy balance for mapping  
1156           evapotranspiration with internalized calibration (METRIC)—model J. Irrig. Drain.  
1157           Eng., 133, pp. 380-394, 10.1061/(ASCE)0733-9437(2007) 133:4(380).
- 1158   Alo, C. A., & Wang, G. (2008). Hydrological impact of the potential future vegetation response to  
1159           climate changes projected by 8 GCMs. *Journal of Geophysical Research: Biogeosciences*,  
1160           113(G3). <https://doi.org/10.1029/2007JG000598>
- 1161   Bair E.H., Rittger K., Davis R.E., Painter T.H., Dozier J. (2016) Validating reconstruction of snow  
1162           water equivalent in California’s Sierra Nevada using measurements from the NASA  
1163           Airborne Snow Observatory *Water Resour. Res.*, 52 , pp. 8437-  
1164           8460, 10.1002/2016WR018704
- 1165   Bales, R. C., Molotch, N. P., Painter, T. H., Dettinger, M. D., Rice, R., & Dozier, J. (2006).  
1166           Mountain hydrology of the western United States. *Water Resources Research*, 42(8).  
1167           <https://doi.org/10.1029/2005WR004387>

1168 Barnett, T. P., Adam, J. C., & Lettenmaier, D. P. (2005). Potential impacts of a warming climate  
1169 on water availability in snow-dominated regions. *Nature*, *438*(7066), 303–309.  
1170 <https://doi.org/10.1038/nature04141>

1171 Berghuijs, W. R., Woods, R. A., & Hrachowitz, M. (2014). A precipitation shift from snow  
1172 towards rain leads to a decrease in streamflow. *Nature Climate Change*, *4*(7), 583–586.  
1173 <https://doi.org/10.1038/nclimate2246>

1174 Bixio, A. C., G. Gambolati, C. Paniconi, M. Putti, V. M. Shestopalov, V. N. Bubljas, A. S.  
1175 Bohuslavsky, N. B. Kastel'seva, and Y. F. Rudenko (2002), Modeling groundwater-  
1176 surface water interactions including effects of morphogenetic depressions in the Chernobyl  
1177 exclusion zone, *Environ. Geol.*, *42*(2-3) 162-177.

1178 Cayan, D. R., Maurer, E. P., Dettinger, M. D., Tyree, M., & Hayhoe, K. (2008). Climate change  
1179 scenarios for the California region. *Climatic Change*, *87*(1), 21–42.  
1180 <https://doi.org/10.1007/s10584-007-9377-6>

1181 Christensen, L., Tague, C. L., & Baron, J. S. (2008). Spatial patterns of simulated transpiration  
1182 response to climate variability in a snow dominated mountain ecosystem. *Hydrological*  
1183 *Processes*, *22*(18), 3576–3588. <https://doi.org/10.1002/hyp.6961>

1184 Collins, W. D., Bitz, C. M., Blackmon, M. L., Bonan, G. B., Bretherton, C. S., Carton, J. A., et al.  
1185 (2006). The Community Climate System Model Version 3 (CCSM3). *Journal of Climate*,  
1186 *19*(11), 2122–2143. <https://doi.org/10.1175/JCLI3761.1>

1187 Condon, L. E., Maxwell, R. M., & Gangopadhyay, S. (2013). The impact of subsurface  
1188 conceptualization on land energy fluxes. *Advances in Water Resources*, *60*, 188–203.  
1189 <https://doi.org/10.1016/j.advwatres.2013.08.001>

1190 Condon, L.E., Atchley, A.L., Maxwell, R.M., (2020). Evapotranspiration depletes groundwater  
1191 under warming over the contiguous United States. *Nature Communications* 11, 873.  
1192 <https://doi.org/10.1038/s41467-020-14688-0>

1193 Cook, E. R., Woodhouse, C. A., Eakin, C. M., Meko, D. M., & Stahle, D. W. (2004). Long-Term  
1194 Aridity Changes in the Western United States. *Science*, 306(5698), 1015–1018.  
1195 <https://doi.org/10.1126/science.1102586>

1196 Coon, E. T., J. D. Moulton, and S. L. Painter (2016), Managing complexity in simulations of land  
1197 surface and near-surface processes, *Environ. Modell Software*, 78, 134-149.

1198 Cosgrove, B. A., Lohmann, D., Mitchell, K. E., Houser, P. R., Wood, E. F., Schaake, J. C., et al.  
1199 (2003). Real-time and retrospective forcing in the North American Land Data Assimilation  
1200 System (NLDAS) project. *Journal of Geophysical Research: Atmospheres*, 108(D22).  
1201 <https://doi.org/10.1029/2002JD003118>

1202 Cristea, N. C., Lundquist, J. D., Loheide, S. P., Lowry, C. S., & Moore, C. E. (2014). Modelling  
1203 how vegetation cover affects climate change impacts on streamflow timing and magnitude  
1204 in the snowmelt-dominated upper Tuolumne Basin, Sierra Nevada. *Hydrological  
1205 Processes*, 28(12), 3896–3918. <https://doi.org/10.1002/hyp.9909>

1206 Daly, C., Halbleib, M., Smith, J. I., Gibson, W. P., Doggett, M. K., Taylor, G. H., et al. (2008).  
1207 Physiographically sensitive mapping of climatological temperature and precipitation across the  
1208 conterminous United States. *International Journal of Climatology*, 28(15), 2031–2064.  
1209 <https://doi.org/10.1002/joc.1688>.

1210 Dettinger, M. (2011). Climate Change, Atmospheric Rivers, and Floods in California – A  
1211 Multimodel Analysis of Storm Frequency and Magnitude Changes1. *JAWRA Journal of*

1212        *the American Water Resources Association*, 47(3), 514–523.  
1213        <https://doi.org/10.1111/j.1752-1688.2011.00546.x>

1214 Dettinger, M., & Anderson, M. L. (2015). Storage in California’s reservoirs and snowpack in this  
1215        time of drought. *San Francisco Estuary and Watershed Science*, 13(2).  
1216        <https://doi.org/10.15447/sfews.2015v13iss2art1>

1217 Dettinger, M., Redmond, K., & Cayan, D. (2004). Winter Orographic Precipitation Ratios in the  
1218        Sierra Nevada—Large-Scale Atmospheric Circulations and Hydrologic Consequences.  
1219        *Journal of Hydrometeorology*, 5(6), 1102–1116. <https://doi.org/10.1175/JHM-390.1>

1220 Dettinger, M. D. (2013). Atmospheric Rivers as Drought Busters on the U.S. West Coast. *Journal*  
1221        *of Hydrometeorology*, 14(6), 1721–1732. <https://doi.org/10.1175/JHM-D-13-02.1>

1222 Di Liberto, T. (2017, October). Very wet 2017 WY ends in California. *NOAA Climate.Gov*.  
1223        Retrieved from [https://www.climate.gov/news-features/featured-images/very-wet-2017-](https://www.climate.gov/news-features/featured-images/very-wet-2017-water-year-ends-california)  
1224        [water-year-ends-california](https://www.climate.gov/news-features/featured-images/very-wet-2017-water-year-ends-california)

1225 Dierauer, J. R., Whitfield, P. H., & Allen, D. M. (2018). Climate Controls on Runoff and Low  
1226        Flows in Mountain Catchments of Western North America. *Water Resources Research*,  
1227        54(10), 7495–7510. <https://doi.org/10.1029/2018WR023087>

1228 Faunt, C.C., Belitz, K., Hanson, R.T., 2010. Development of a three-dimensional model of  
1229        sedimentary texture in valley-fill deposits of Central Valley, California, USA.  
1230        *Hydrogeology Journal* 18, 625–649. <https://doi.org/10.1007/s10040-009-0539-7>

1231 Faunt, C.C., Geological Survey (U.S.) (Eds.), 2009. Groundwater availability of the Central Valley  
1232        Aquifer, California, U.S. Geological Survey professional paper. U.S. Geological Survey,  
1233        Reston, Va.



1234 Ferguson, I. M. and Maxwell, R. M. (2010). Role of groundwater in watershed response and land  
1235 surface feedbacks under climate change. *Water Resour. Res.*, 46, 1–  
1236 15. <https://doi.org/10.1029/2009WR008616>.

1237 Ficklin, D. L., Luo, Y., & Zhang, M. (2013). Climate change sensitivity assessment of streamflow  
1238 and agricultural pollutant transport in California’s Central Valley using Latin hypercube  
1239 sampling. *Hydrological Processes*, 27(18), 2666–2675. <https://doi.org/10.1002/hyp.9386>

1240 Foster, L. M., Williams, K. H., & Maxwell, R. M. (2020). Resolution matters when modeling  
1241 climate change in headwaters of the Colorado River. *Environmental Research Letters*.  
1242 <https://doi.org/10.1088/1748-9326/aba77f>

1243 Gates WL (1992) AMIP: the atmospheric model intercomparison project. *Bull Am Meteorol Soc*  
1244 73(12):1962–1970. doi:10.1175/1520-0477(1992)073<1962:ATAMIP>2.0.CO;2

1245 Geologic Map of California, 2015. Geologic Map of California [WWW Document]. Geologic Map  
1246 of California. URL <https://maps.conservation.ca.gov/cgs/gmc/> (accessed 10.17.18).

1247 Gent, P. R., Danabasoglu, G., Donner, L. J., Holland, M. M., Hunke, E. C., Jayne, S. R., et al.  
1248 (2011). The Community Climate System Model Version 4. *Journal of Climate*, 24(19),  
1249 4973–4991. <https://doi.org/10.1175/2011JCLI4083.1>

1250 Gershunov, A., Shulgina, T., Clemesha, R.E.S. et al. (2019). Precipitation regime change in  
1251 Western North America: The role of Atmospheric Rivers. *Sci Rep* 9, 9944.  
1252 <https://doi.org/10.1038/s41598-019-46169-w>

1253 Gettelman, A., and Morrison, H. (2015). Advanced Two-Moment Bulk Microphysics for Global  
1254 Models. Part I: Off-Line Tests and Comparison with Other Schemes. *Journal of Climate*  
1255 28, 3, 1268-1287. <https://doi.org/10.1175/JCLI-D-14-00102.1>

Formatted: Font: (Default) Times New Roman, 12 pt, Font color: Text 1, Pattern: Clear

Formatted: Font: (Default) Times New Roman, 12 pt, Font color: Text 1, Pattern: Clear

Formatted: Font color: Text 1

Formatted: Font: (Default) Times New Roman, 12 pt, Font color: Text 1, Pattern: Clear

1256 Gilbert, J.M., Maxwell, R.M., 2017. Examining regional groundwater - surface water dynamics  
1257 using an integrated hydrologic model of the San Joaquin River basin. *Hydrology and Earth*  
1258 *System Sciences* 21, 923–947. <https://doi.org/10.5194/hess-21-923-2017>

1259 Gleick, P. H. (1987). The development and testing of a water balance model for climate impact  
1260 assessment: Modeling the Sacramento Basin. *Water Resources Research*, 23(6), 1049–  
1261 1061. <https://doi.org/10.1029/WR023i006p01049>

1262 Godsey, S. E., Kirchner, J. W., & Tague, C. L. (2014). Effects of changes in winter snowpacks on  
1263 summer low flows: case studies in the Sierra Nevada, California, USA. *Hydrological*  
1264 *Processes*, 28(19), 5048–5064. <https://doi.org/10.1002/hyp.9943>

1265 Griffin, D., & Anchukaitis, K. J. (2014). How unusual is the 2012–2014 California drought?  
1266 *Geophysical Research Letters*, 41(24), 9017–9023.  
1267 <https://doi.org/10.1002/2014GL062433>

1268 Haarsma, R. J., Roberts, M. J., Vidale, P. L., Senior, C. A., Bellucci, A., Bao, Q., Chang, P., Corti,  
1269 S., Fučkar, N. S., Guemas, V., von Hardenberg, J., Hazeleger, W., Kodama, C., Koenigk,  
1270 T., Leung, L. R., Lu, J., Luo, J.-J., Mao, J., Mizielinski, M. S., Mizuta, R., Nobre, P., Satoh,  
1271 M., Scoccimarro, E., Semmler, T., Small, J., and von Storch, J.-S. (2016). High Resolution  
1272 Model Intercomparison Project (HighResMIP v1.0) for CMIP6, *Geosci. Model Dev.*, 9,  
1273 4185–4208, <https://doi.org/10.5194/gmd-9-4185-2016>.

1274 Harbaugh AW (2005) MODFLOW-2005, The U.S. Geological Survey modular ground-water  
1275 model: the ground-water flow process. US Geol Surv Tech Methods 6-  
1276 A16. <http://pubs.usgs.gov/tm/2005/tm6A16/>.

- 1277 Harpold, A. A., & Molotch, N. P. (2015). Sensitivity of soil water availability to changing  
1278 snowmelt timing in the western U.S. *Geophysical Research Letters*, *42*(19), 8011–8020.  
1279 <https://doi.org/10.1002/2015GL065855>
- 1280 Hayhoe, K., Cayan, D., Field, C. B., Frumhoff, P. C., Maurer, E. P., Miller, N. L., et al. (2004).  
1281 Emissions pathways, climate change, and impacts on California. *Proceedings of the*  
1282 *National Academy of Sciences*, *101*(34), 12422–12427.  
1283 <https://doi.org/10.1073/pnas.0404500101>
- 1284 He, M., Anderson, M., Schwarz, A., Das, T., Lynn, E., Anderson, J., et al. (2019). Potential  
1285 Changes in Runoff of California’s Major Water Supply Watersheds in the 21st Century.  
1286 *Water*, *11*(8), 1651. <https://doi.org/10.3390/w11081651>
- 1287 Herrington, A. R., P. H. Lauritzen, M. A. Taylor, S. Goldhaber, B. E. Eaton, J. T. Bacmeister, K.  
1288 A. Reed, and P. A. Ullrich (2019). Physics–Dynamics Coupling with Element-Based High-  
1289 Order Galerkin Methods: Quasi-Equal-Area Physics Grid. *Mon. Wea. Rev.*, *147*, 69–84,  
1290 <https://doi.org/10.1175/MWR-D-18-0136.1>.
- 1291 Homer, C., Dewitz, J., Yang, L., Jin, S., Danielson, P., Xian, G., et al. (2015). Completion of the  
1292 2011 National Land Cover Database for the conterminous United States—representing a  
1293 decade of land cover change information. *Photogrammetric Engineering & Remote*  
1294 *Sensing*, *81*(5), 345–354.
- 1295 Huang, X., Rhoades, A. M., Ullrich, P. A., & Zarzycki, C. M. (2016). An evaluation of the  
1296 variable-resolution CESM for modeling California’s climate. *Journal of Advances in*  
1297 *Modeling Earth Systems*, *8*(1), 345–369. <https://doi.org/10.1002/2015MS000559>
- 1298 Huang, X., Stevenson, S., & Hall, A. D. (2020). Future warming and intensification of  
1299 precipitation extremes: A “double whammy” leading to increasing flood risk in California.

1300 Geophysical Research Letters, 47, e2020GL088679.  
1301 <https://doi.org/10.1029/2020GL088679>

1302 Hurrell, J. W., Holland, M. M., Gent, P. R., Ghan, S., Kay, J. E., Kushner, P. J., et al. (2013). The  
1303 Community Earth System Model: A Framework for Collaborative Research. *Bulletin of*  
1304 *the American Meteorological Society*, 94(9), 1339–1360. <https://doi.org/10.1175/BAMS->  
1305 [D-12-00121.1](https://doi.org/10.1175/BAMS-D-12-00121.1)

1306 Hurst. (1951) Long-Term Storage Capacity of Reservoirs. *Trans. Am. Soc. Civ. Eng.*, 116, 770–  
1307 799.

1308 Jones, P. W., (1999). First- and Second-Order Conservative Remapping Schemes for Grids in  
1309 Spherical Coordinates. *Mon. Wea. Rev.*, 127, 2204–2210, <https://doi.org/10.1175/1520->  
1310 [0493\(1999\)127<2204:FASOCR>2.0.CO;2](https://doi.org/10.1175/1520-0493(1999)127<2204:FASOCR>2.0.CO;2).

1311 IGBP, 2018. Global plant database published - IGBP [WWW Document]. URL  
1312 <http://www.igbp.net/news/news/news/globalplantdatabasepublished.5.1b8ae20512db692f>  
1313 [2a6800014762.html](http://www.igbp.net/news/news/news/globalplantdatabasepublished.5.1b8ae20512db692f) (accessed 10.17.18).

1314 Jennings, C. W., Strand, R. G., & Rogers, T. H. (1977). Geologic map of California. Sacramento,  
1315 Calif.: Division of Mines and Geology.

1316 Kampenhout, L. van, Rhoades, A. M., Herrington, A. R., Zarzycki, C. M., Lenaerts, J. T. M.,  
1317 Sacks, W. J., & Broeke, M. R. van den. (2019). Regional grid refinement in an Earth system  
1318 model: impacts on the simulated Greenland surface mass balance. *The Cryosphere*, 13(6),  
1319 1547–1564. <https://doi.org/10.5194/tc-13-1547-2019>

1320 Kollet, S. J., & Maxwell, R. M. (2006). Integrated surface–groundwater flow modeling: A free-  
1321 surface overland flow boundary condition in a parallel groundwater flow model. *Advances*  
1322 *in Water Resources*, 29(7), 945–958. <https://doi.org/10.1016/j.advwatres.2005.08.006>

Formatted: Font color: Text 1

Formatted: Font color: Text 1

1323 [Koutsoyiannis, D. \(2003\) Climate change, the Hurst phenomenon, and hydrological statistics,](#)  
1324 [Hydrological Sciences Journal, 48:1, 3-24, DOI: 10.1623/hysj.48.1.3.43481](#)

1325 [Koutsoyiannis, D., \(2020\) Revisiting the global hydrological cycle: is it intensifying?, Hydrology](#)  
1326 [and Earth System Sciences, 24, 3899–3932, doi:10.5194/hess-24-3899-2020.](#)

1327 [La Follette, P. T., Teuling, A. J., Addor, N., Clark, M., Jansen, K., & Melsen, L. A. \(2021\).](#)  
1328 [Numerical daemons of hydrological models are summoned by extreme precipitation.](#)  
1329 [Hydrology and Earth System Sciences, 25\(10\), 5425–5446. https://doi.org/10.5194/hess-](#)  
1330 [25-5425-2021](#)

1331 [Lehner, F., Deser, C., Maher, N., Marotzke, J., Fischer, E. M., Brunner, L., et al. \(2020\).](#)  
1332 [Partitioning climate projection uncertainty with multiple large ensembles and CMIP5/6.](#)  
1333 [Earth System Dynamics, 11\(2\), 491–508. https://doi.org/10.5194/esd-11-491-2020.](#)

1334 Lemordant, L., Gentine, P., Swann, A. S., Cook, B. I., & Scheff, J. (2018). Critical impact of  
1335 vegetation physiology on the continental hydrologic cycle in response to increasing CO<sub>2</sub>.  
1336 *Proceedings of the National Academy of Sciences*, 115(16), 4093–4098.  
1337 <https://doi.org/10.1073/pnas.1720712115>

1338 Liang, X., D. P. Lettenmaier, E. F. Wood, and S. J. Burges (1994), A simple hydrologically based  
1339 model of land surface water and energy fluxes for general circulation models, *J. Geophys.*  
1340 *Res.*, 99(D7), 14415–14428, doi:10.1029/94JD00483.

1341 [Lundquist, J. D., Hughes, M., Henn, B., Gutmann, E. D., Livneh, B., Dozier, J., & Neiman, P.](#)  
1342 (2015). High-Elevation Precipitation Patterns: Using Snow Measurements to Assess Daily  
1343 Gridded Datasets across the Sierra Nevada, California, *Journal of Hydrometeorology*,  
1344 16(4), 1773-1792. doi: [https://journals.ametsoc.org/view/journals/hydr/16/4/jhm-d-15-](https://journals.ametsoc.org/view/journals/hydr/16/4/jhm-d-15-0019_1.xml)  
1345 [0019\\_1.xml](https://journals.ametsoc.org/view/journals/hydr/16/4/jhm-d-15-0019_1.xml)

Formatted: Font: (Default) Times New Roman, 12 pt, Not Italic

Formatted: Normal, Indent: Left: 0", Hanging: 0.5"

Formatted: Font: Not Italic

Formatted: Font: Not Italic

Formatted: Font: Not Italic

Formatted: Font: Not Italic

Formatted: Font color: Auto

Deleted: ¶

1347 Maina, Fadji Z., Siirila-Woodburn, E. R., Newcomer, M., Xu, Z., & Steefel, C. (2020a).  
1348 Determining the impact of a severe dry to wet transition on watershed hydrodynamics in  
1349 California, USA with an integrated hydrologic model. *Journal of Hydrology*, 580, 124358.  
1350 <https://doi.org/10.1016/j.jhydrol.2019.124358>

1351 Maina, F. Z., Siirila-Woodburn, E. R., & Vahmani, P. (2020b). Sensitivity of meteorological-  
1352 forcing resolution on hydrologic variables. *Hydrology and Earth System Sciences*, 24(7),  
1353 3451–3474. <https://doi.org/10.5194/hess-24-3451-2020>

1354 Maina, Fadji Zaoua, & Siirila-Woodburn, E. R. (2020c). Watersheds dynamics following  
1355 wildfires: Nonlinear feedbacks and implications on hydrologic responses. *Hydrological*  
1356 *Processes*, 34(1), 33–50. <https://doi.org/10.1002/hyp.13568>

1357 ~~Maina, Fadji Z., Siirila-Woodburn, E. R., & Dennedy-Frank, P. J. (2022) Assessing the impacts of~~  
1358 ~~[hydrodynamic parameter uncertainties on simulated evapotranspiration in a mountainous](#)~~  
1359 ~~[watershed. \*Journal of Hydrology\* 608. <https://doi.org/10.1016/j.jhydrol.2022.127620>.](#)~~

1360 Mallakpour, I., Sadegh, M., AghaKouchak, A., 2018. A new normal for streamflow in California  
1361 in a warming climate: Wetter wet seasons and drier dry seasons. *Journal of Hydrology* 567,  
1362 203–211. <https://doi.org/10.1016/j.jhydrol.2018.10.023>

1363 Maurer, E. P. (2007). Uncertainty in hydrologic impacts of climate change in the Sierra Nevada,  
1364 California, under two emissions scenarios. *Climatic Change*, 82(3), 309–325.  
1365 <https://doi.org/10.1007/s10584-006-9180-9>

1366 Maurer, E. P., & Duffy, P. B. (2005). Uncertainty in projections of streamflow changes due to  
1367 climate change in California. *Geophysical Research Letters*, 32(3).  
1368 <https://doi.org/10.1029/2004GL021462>

Deleted: ¶

1370 Maxwell, R. M. (2013). A terrain-following grid transform and preconditioner for parallel, large-  
1371 scale, integrated hydrologic modeling. *Advances in Water Resources*, 53, 109–117.  
1372 <https://doi.org/10.1016/j.advwatres.2012.10.001>

1373 Maxwell, R. M., & Condon, L. E. (2016). Connections between groundwater flow and  
1374 transpiration partitioning. *Science*, 353(6297), 377–380.  
1375 <https://doi.org/10.1126/science.aaf7891>

1376 Maxwell, R. M., & Miller, N. L. (2005). Development of a Coupled Land Surface and  
1377 Groundwater Model. *Journal of Hydrometeorology*, 6(3), 233–247.  
1378 <https://doi.org/10.1175/JHM422.1>

1379 Mayer, T. D., & Naman, S. W. (2011). Streamflow Response to Climate as Influenced by Geology  
1380 and Elevation1. *JAWRA Journal of the American Water Resources Association*, 47(4),  
1381 724–738. <https://doi.org/10.1111/j.1752-1688.2011.00537.x>Boryan, C., Yang, Z.,  
1382 Mueller, R., Craig, M., 2011. Monitoring US agriculture: the US Department of  
1383 Agriculture, National Agricultural Statistics Service, Cropland Data Layer Program.  
1384 Geocarto International 26, 341–358. <https://doi.org/10.1080/10106049.2011.562309>

1385 Mallakpour, I., Sadegh, M., AghaKouchak, A., 2018. A new normal for streamflow in California  
1386 in a warming climate: Wetter wet seasons and drier dry seasons. *Journal of Hydrology* 567,  
1387 203–211. <https://doi.org/10.1016/j.jhydrol.2018.10.023>

1388 Maxwell, R.M., 2013. A terrain-following grid transform and preconditioner for parallel, large-  
1389 scale, integrated hydrologic modeling. *Advances in Water Resources* 53, 109–117.  
1390 <https://doi.org/10.1016/j.advwatres.2012.10.001>

1391 McEvoy, D.J., Pierce, D.W., Kalansky, J.F., Cayan, D.R., Abatzoglou, J.T., 2020. Projected  
1392 Changes in Reference Evapotranspiration in California and Nevada: Implications for

1393 Drought and Wildland Fire Danger. *Earth's Future* 8, e2020EF001736.  
1394 <https://doi.org/10.1029/2020EF001736>

1395 Milly, P. C. D., & Dunne, K. A. (2017). A Hydrologic Drying Bias in Water-Resource Impact  
1396 Analyses of Anthropogenic Climate Change. *JAWRA Journal of the American Water*  
1397 *Resources Association*, 53(4), 822–838. <https://doi.org/10.1111/1752-1688.12538>

1398 Milly, P. C. D., Dunne, K. A., & Vecchia, A. V. (2005). Global pattern of trends in streamflow  
1399 and water availability in a changing climate. *Nature*, 438(7066), 347–350.  
1400 <https://doi.org/10.1038/nature04312>

1401 Mote, P. W., Hamlet, A. F., Clark, M. P., & Lettenmaier, D. P. (2005). Declining mountain  
1402 snowpack in western north america\*. *Bulletin of the American Meteorological Society*,  
1403 86(1), 39–50. <https://doi.org/10.1175/BAMS-86-1-39>

1404 Musselman, K. N., Clark, M. P., Liu, C., Ikeda, K., & Rasmussen, R. (2017). Slower snowmelt in  
1405 a warmer world. *Nature Climate Change*, 7(3), 214–219.  
1406 <https://doi.org/10.1038/nclimate3225>

1407 Musselman, K. N., Molotch, N. P., & Margulis, S. A. (2017). Snowmelt response to simulated  
1408 warming across a large elevation gradient, southern Sierra Nevada, California. *The*  
1409 *Cryosphere*, 11(6), 2847–2866. <https://doi.org/10.5194/tc-11-2847-2017>

1410 National Operational Hydrologic Remote Sensing Center. (2004). Snow Data Assimilation  
1411 System (SNODAS) Data Products at NSIDC. <https://doi.org/10.7265/N5TB14TC>.

1412 Neelin, J. D., Langenbrunner, B., Meyerson, J. E., Hall, A., & Berg, N. (2013). California Winter  
1413 Precipitation Change under Global Warming in the Coupled Model Intercomparison  
1414 Project Phase 5 Ensemble. *Journal of Climate*, 26(17), 6238–6256.  
1415 <https://doi.org/10.1175/JCLI-D-12-00514.1>



1416 Neitsch, S. L., Arnold, J. G., Kiniry, J. R., & Williams, J. R. (2001). Soil and Water Assessment  
1417 tool (SWAT) user's manual version 2000. Grassland Soil and Water Research Laboratory.  
1418 Temple, TX: ARS.

1419 Niraula, R., Meixner, T., Dominguez, F., Bhattarai, N., Rodell, M., Ajami, H., et al. (2017). How  
1420 Might Recharge Change Under Projected Climate Change in the Western U.S.?  
1421 *Geophysical Research Letters*, 44(20), 10,407-10,418.  
1422 <https://doi.org/10.1002/2017GL075421>

1423 Niu, G.-Y., et al. (2011), The community Noah land surface model with multiparameterization  
1424 options (Noah-MP): 1. Model description and evaluation with local-scale measurements. *J.*  
1425 *Geophys. Res.*, 116, D12109, doi: 10.1029/2010JD015139.

1426 SMAP. (2015). Soil Moisture Active Passive. Retrieved October 18, 2018, from SMAP  
1427 website: <https://smap.jpl.nasa.gov/>

1428 Siirila-Woodburn, E. R., Rhoades, A. M., Hatchett, B. J., Huning, L. S., Szinai, J., Tague, C., Nico,  
1429 P. S., Feldman, D. R., Jones, A. D., Collins, W. D., and Kaatz, L.: A low-to-no snow future  
1430 and its impacts on water resources in the western United States, *Nature Reviews Earth and*  
1431 *Environment*, <https://doi.org/10.1038/s43017-021-00219-y>, 2021.

1432 Pascolini-Campbell, M., Reager, J. T., Chandanpurkar, H. A., & Rodell, M. (2021). A 10 per cent  
1433 increase in global land evapotranspiration from 2003 to 2019. *Nature*, 593(7860), 543–547.  
1434 <https://doi.org/10.1038/s41586-021-03503-5>

1435 Payne, A. E., Demory, M.-E., Leung, L. R., Ramos, A. M., Shields, C. A., Rutz, J. J., et al. (2020).  
1436 Responses and impacts of atmospheric rivers to climate change. *Nature Reviews Earth &*  
1437 *Environment*, 1(3), 143–157. <https://doi.org/10.1038/s43017-020-0030-5>

1438 Persad, G. G., Swain, D. L., Kouba, C., & Ortiz-Partida, J. P. (2020). Inter-model agreement on  
1439 projected shifts in California hydroclimate characteristics critical to water management.  
1440 *Climatic Change*, 162(3), 1493–1513. <https://doi.org/10.1007/s10584-020-02882-4>

1441 Ralph, F. M., & Dettinger, M. D. (2011). Storms, floods, and the science of atmospheric rivers.  
1442 *Eos, Transactions American Geophysical Union*, 92(32), 265–266.  
1443 <https://doi.org/10.1029/2011EO320001>

1444 Ralph, F. Martin, Neiman, P. J., Wick, G. A., Gutman, S. I., Dettinger, M. D., Cayan, D. R., &  
1445 White, A. B. (2006). Flooding on California’s Russian River: Role of atmospheric rivers.  
1446 *Geophysical Research Letters*, 33(13). <https://doi.org/10.1029/2006GL026689>

1447 Rasmussen, R., Liu, C., Ikeda, K., Gochis, D., Yates, D., Chen, F., et al. (2011). High-Resolution  
1448 Coupled Climate Runoff Simulations of Seasonal Snowfall over Colorado: A Process  
1449 Study of Current and Warmer Climate. *Journal of Climate*, 24(12), 3015–3048.  
1450 <https://doi.org/10.1175/2010JCLI3985.1>

1451 Rhoades, A. M., Huang, X., Ullrich, P. A., & Zarzycki, C. M. (2016). Characterizing Sierra Nevada  
1452 Snowpack Using Variable-Resolution CESM. *Journal of Applied Meteorology and  
1453 Climatology*, 55(1), 173–196. <https://doi.org/10.1175/JAMC-D-15-0156.1>

1454 Rhoades, A. M., Ullrich, P. A., & Zarzycki, C. M. (2018a). Projecting 21st century snowpack  
1455 trends in western USA mountains using variable-resolution CESM. *Climate Dynamics*,  
1456 50(1), 261–288. <https://doi.org/10.1007/s00382-017-3606-0>

1457 Rhoades, A. M., Jones, A. D., & Ullrich, P. A. (2018b). The changing character of the California  
1458 Sierra Nevada as a natural reservoir. *Geophysical Research Letters*, 45, 13,008– 13,019.  
1459 <https://doi.org/10.1029/2018GL080308>

Deleted: ¶

1461 Rhoades, A. M., Ullrich, P. A., Zarzycki, C. M., Johansen, H., Margulis, S. A., Morrison, H., et  
1462 al. (2018c). Sensitivity of Mountain Hydroclimate Simulations in Variable-Resolution  
1463 CESM to Microphysics and Horizontal Resolution. *Journal of Advances in Modeling Earth*  
1464 *Systems*, 10(6), 1357–1380. <https://doi.org/10.1029/2018MS001326>

1465 Rhoades, A. M., Jones, A. D., O'Brien, T. A., O'Brien, J. P., Ullrich, P. A., & Zarzycki, C. M.  
1466 (2020a). Influences of North Pacific Ocean domain extent on the western U.S. winter  
1467 hydroclimatology in variable-resolution CESM. *Journal of Geophysical Research:*  
1468 *Atmospheres*, 125, e2019JD031977. <https://doi.org/10.1029/2019JD031977>

1469 Rhoades, A. M., Jones, A. D., Srivastava, A., Huang, H., O'Brien, T. A., Patricola, C. M., et al.  
1470 (2020b). The shifting scales of western U.S. landfalling atmospheric rivers under climate  
1471 change. *Geophysical Research Letters*, 47, e2020GL089096.  
1472 <https://doi.org/10.1029/2020GL089096>

1473 Rhoades, A. M., Risser, M. D., Stone, D. A., Wehner, M. F., & Jones, A. D. (2021). Implications  
1474 of warming on western United States landfalling atmospheric rivers and their flood  
1475 damages. *Weather and Climate Extremes*, 32, 100326,  
1476 <https://doi.org/10.1016/j.wace.2021.100326>

1477 Richards, L. A. (1931). Capillary conduction of liquids through porous medium. *Journal of*  
1478 *Applied Physics*, 1(5), 318–333. <https://doi.org/10.1063/1.1745010>

1479 Safeeq, M., Grant, G. E., Lewis, S. L., Kramer, M. G., & Staab, B. (2014). A hydrogeologic  
1480 framework for characterizing summer streamflow sensitivity to climate warming in the  
1481 Pacific Northwest, USA. *Hydrology and Earth System Sciences*, (18), 1–8.  
1482 <https://doi.org/10.5194/hess-18-3693-2014>

1483 Safeeq, M., Grant, G.E., Lewis, S.L. and Tague, C.L. (2013), Coupling snowpack and groundwater  
1484 dynamics to interpret historical streamflow trends in the western United States. *Hydrol.*  
1485 *Process.*, 27: 655-668. <https://doi.org/10.1002/hyp.9628>

1486 Safeeq, Mohammad, Grant, G. E., Lewis, S. L., & Staab, B. (2015). Predicting landscape  
1487 sensitivity to present and future floods in the Pacific Northwest, USA. *Hydrological*  
1488 *Processes*, 29(26), 5337–5353. <https://doi.org/10.1002/hyp.10553>

1489 SCRIPPS Institution of Oceanography. (2017, April). Northern California Just Surpassed the  
1490 Wettest Year on Record | Scripps Institution of Oceanography, UC San Diego. Retrieved  
1491 from <https://scripps.ucsd.edu/news/northern-california-just-surpassed-wettest-year-record>

1492 Shukla, S., Safeeq, M., AghaKouchak, A., Guan, K., & Funk, C. (2015). Temperature impacts on  
1493 the WY 2014 drought in California. *Geophysical Research Letters*, 4384–4393.  
1494 [https://doi.org/10.1002/2015GL063666@10.1002/\(ISSN\)1944-8007.CALDROUGHT1](https://doi.org/10.1002/2015GL063666@10.1002/(ISSN)1944-8007.CALDROUGHT1)

1495 Son, K., & Tague, C. (2019). Hydrologic responses to climate warming for a snow-dominated  
1496 watershed and a transient snow watershed in the California Sierra. *Ecohydrology*, 12(1),  
1497 e2053. <https://doi.org/10.1002/eco.2053>

1498 [Song, X., Zhang, J., Zhan, C., Xuan, Y., Ye, M., Xu C. \(2015\) Global sensitivity analysis in](#)  
1499 [hydrological modeling: Review of concepts, methods, theoretical framework, and](#)  
1500 [applications. \*Journal of Hydrology\*, 523, pp. 739-757, 10.1016/j.jhydrol.2015.02.013](#)

1501 Strachan, S., and Daly, C. (2017), Testing the daily PRISM air temperature model on semiarid  
1502 mountain slopes, *J. Geophys. Res. Atmos.*, 122, 5697– 5715, doi:10.1002/2016JD025920.

1503 Swain, D. L., Langenbrunner, B., Neelin, J. D., & Hall, A. (2018). Increasing precipitation  
1504 volatility in twenty-first-century California. *Nature Climate Change*, 8(5), 427–433.  
1505 <https://doi.org/10.1038/s41558-018-0140-y>

Formatted: Font: Times New Roman, Font color: Text 1

Formatted: Font: Times New Roman, Font color: Text 1

Formatted: Default Paragraph Font, Font: Times New Roman, Font color: Text 1

Formatted: Font: Times New Roman, Font color: Text 1

Formatted: Default Paragraph Font, Font: Times New Roman, Font color: Text 1

Formatted: Font: Times New Roman, Font color: Text 1

Formatted: Default Paragraph Font, Font: Times New Roman, Font color: Text 1

Formatted: Font: Times New Roman, Font color: Text 1

Formatted: Default Paragraph Font, Font: Times New Roman, Font color: Text 1

Formatted: Font: Times New Roman, Font color: Text 1

Formatted: Default Paragraph Font, Font: Times New Roman, Font color: Text 1

Formatted: Font: Times New Roman, Font color: Text 1

Formatted: Default Paragraph Font, Font: Times New Roman, Font color: Text 1

Formatted: Font: Times New Roman, Font color: Text 1

Formatted: Default Paragraph Font, Font: Times New Roman, Font color: Text 1

Formatted: Font: Times New Roman, Font color: Text 1

Formatted: Default Paragraph Font, Font: Times New Roman, Font color: Text 1

Formatted: Font: Times New Roman, Font color: Text 1

Formatted: Default Paragraph Font, Font: Times New Roman, Font color: Text 1

Formatted: Font: Times New Roman, Font color: Text 1

1506 Tague, C., & Peng, H. (2013). The sensitivity of forest water use to the timing of precipitation and  
1507 snowmelt recharge in the California Sierra: Implications for a warming climate. *Journal of*  
1508 *Geophysical Research: Biogeosciences*, 118(2), 875–887.  
1509 <https://doi.org/10.1002/jgrg.20073>

1510 Tang, G., Li, S., Yang, M., Xu, Z., Liu, Y., & Gu, H. (2019). Streamflow response to snow regime  
1511 shift associated with climate variability in four mountain watersheds in the US Great Basin.  
1512 *Journal of Hydrology*, 573, 255–266. <https://doi.org/10.1016/j.jhydrol.2019.03.021>

1513 The NCAR Command Language (Version 6.6.2) (2021). Boulder, Colorado:  
1514 UCAR/NCAR/CISL/TDD, 851 <http://dx.doi.org/10.5065/D6WD3XH5>.

1515 Trefry, M.G.; Muffels, C. (2007). "FEFLOW: a finite-element ground water flow and transport  
1516 modeling tool". *Ground Water*. 45 (5): 525–528. doi:10.1111/j.1745-6584.2007.00358.x

1517 Vicuna, S., & Dracup, J. A. (2007). The evolution of climate change impact studies on hydrology  
1518 and water resources in California. *Climatic Change*, 82(3), 327–350.  
1519 <https://doi.org/10.1007/s10584-006-9207-2>

1520 Vicuna, Sebastian, Maurer, E. P., Joyce, B., Dracup, J. A., & Purkey, D. (2007). The Sensitivity  
1521 of California Water Resources to Climate Change Scenarios1. *JAWRA Journal of the*  
1522 *American Water Resources Association*, 43(2), 482–498. [https://doi.org/10.1111/j.1752-](https://doi.org/10.1111/j.1752-1688.2007.00038.x)  
1523 [1688.2007.00038.x](https://doi.org/10.1111/j.1752-1688.2007.00038.x)

1524 Wang, S.-Y. S., Yoon, J.-H., Becker, E., & Gillies, R. (2017). California from drought to deluge.  
1525 *Nature Climate Change*, 7(7), 465. <https://doi.org/10.1038/nclimate3330>

1526 Welch, L.A., Allen, D.M., 2014. Hydraulic conductivity characteristics in mountains and  
1527 implications for conceptualizing bedrock groundwater flow. *Hydrogeol J* 22, 1003–1026.  
1528 <https://doi.org/10.1007/s10040-014-1121-5>

1529 Wu, C., Liu, X., Lin, Z., Rhoades, A. M., Ullrich, P. A., Zarzycki, C. M., et al. (2017). Exploring  
1530 a Variable-Resolution Approach for Simulating Regional Climate in the Rocky Mountain  
1531 Region Using the VR-CESM. *Journal of Geophysical Research: Atmospheres*, 122(20),  
1532 10,939-10,965. <https://doi.org/10.1002/2017JD027008>  
1533 Zarzycki, C. M., Levy, M. N., Jablonowski, C., Overfelt, J. R., Taylor, M. A., and Ullrich, P. A.  
1534 (2014). Aquaplanet Experiments Using CAM's Variable-Resolution Dynamical Core.  
1535 *Journal of Climate* 27, 14, 5481-5503, <https://doi.org/10.1175/JCLI-D-14-00004.1>  
1536  
1537  
1538  
1539